JOURNAL OF GEOPHYSICAL RESEARCH, VOL. 114, D01102, doi:10.1029/2008JD010374, 2009

Global distribution of atmospheric waves in the equatorial upper troposphere and lower stratosphere: AGCM simulation of sources and propagation

Yoshio Kawatani,[1] Masaaki Takahashi,[1,2] Kaoru Sato,[3] Simon P. Alexander,[4,5] and Toshitaka Tsuda[4]

Received 6 May 2008; revised 8 October 2008; accepted 29 October 2008; published 9 January 2009.

[1] The global distribution, sources, and propagation of atmospheric waves in the equatorial upper troposphere and lower stratosphere were investigated using an atmospheric general circulation model with T106L60 resolution (120-km horizontal and 550-m vertical resolution). The quasibiennial oscillation (QBO) with a period of $\sim$1.5–2 years was simulated well without gravity wave drag parameterization. The zonal wave number versus the frequency spectra of simulated precipitation represent realistic signals of convectively coupled equatorial trapped waves (EQWs). The temperature spectra in the stratosphere also indicate dominant signals of EQWs. EQWs with equivalent depths in the range of 8–90 m from the $n = -1$ mode to $n = 2$ mode were extracted separately. Each EQW in the stratosphere generally corresponded well with the source of each convectively coupled EQW activity in the troposphere. The propagations of Kelvin waves and $n = 0$ eastward/westward propagating EQWs are strongly influenced by the Walker circulation and the phase of the QBO. Potential energy associated with EQWs is generally larger in the westerly than in the easterly shear phase of the QBO. EQWs with vertical wavelengths $\leq$ 7 km contribute up to $\sim$30% of total potential energy $\leq$ 7 km over the equator at an altitude of 20–30 km. Gravity waves generated by cumulus convection with periods $\leq$ 24 h are clearly visible over areas of Africa, the Amazon, and around Indonesia, and result in localized PE distributions in areas short distances from the source region. Comparisons of the model results and recent satellite observations are discussed.

Citation: Kawatani, Y., M. Takahashi, K. Sato, S. P. Alexander, and T. Tsuda (2009), Global distribution of atmospheric waves in the equatorial upper troposphere and lower stratosphere: AGCM simulation of sources and propagation, *J. Geophys. Res.*, *114*, D01102, doi:10.1029/2008JD010374.

1. Introduction

[2] Numerous observational, theoretical, and modeling studies have shown that energy and momentum transports by gravity waves have important effects on the large-scale circulation and thermal structure of the middle atmosphere [*Fritts and Alexander*, 2003]. In addition to stationary gravity waves induced by mountains, nonstationary gravity waves are generated by convection, fronts, and jets [*Fritts and Nastrom*, 1992]. In the equatorial region, convectively generated waves make the most important contribution to gravity-wave drag [*Horinouchi et al.*, 2002, 2003]. The quasibiennial oscillation (QBO) in the equatorial lower stratosphere is thought to be driven by atmospheric waves, such as equatorial trapped waves (EQWs) and three-dimensionally propagating gravity waves (3D-gravity waves) through wave-mean flow interaction [*Sato and Dunkerton*, 1997; *Horinouchi and Yoden*, 1998; *Baldwin et al.*, 2001]. Atmospheric waves over the equatorial region also contribute to driving the stratopause and mesopause semi-annual oscillation (SAO) and the mesospheric QBO [*Baldwin et al.*, 2001].

[3] Ground-based observational instruments such as radiosondes [e.g., *Allen and Vincent*, 1995; *Yoshiki and Sato*, 2000], rockets [e.g., *Hirota*, 1984; *Hamilton*, 1991; *Eckermann et al.*, 1995], and radar [e.g., *Tsuda et al.*, 1990; *Sato*, 1994; *Dhaka et al.*, 2003] are used to study atmospheric waves. For example, Kelvin waves and mixed Rossby-gravity (MRG) waves were discovered by radiosonde observations [*Wallace and Kousky*, 1968; *Yanai and Maruyama*, 1966]. *Wada et al.* [1999] used radiosonde measurements of horizontal winds and temperature taken

[1]Frontier Research Center for Global Change, Japan Agency for Marine-Earth Science and Technology, Yokohama, Japan.
[2]Center for Climate System Research, University of Tokyo, Kashiwa, Japan.
[3]Department of Earth and Planetary Science, Graduate School of Science, University of Tokyo, Tokyo, Japan.
[4]Research Institute for Sustainable Humanosphere, Kyoto University, Kyoto, Japan.
[5]Australian Antarctic Division, Kingston, Tasmania, Australia.

0148-0227/09/2008JD010374$09.00

at 10 stations during the Tropical Ocean Global Atmosphere Coupled Ocean Atmosphere Response Experiment (TOGA-COARE) intensive observational period to reveal $n = 0$ and $n = 1$ eastward-propagating inertia-gravity waves (n is the order of the solution for the dispersion relation of EQWs; see equation (4) in section 3). Ground-based instruments can also provide information on momentum flux because they can observe wind components. However, most observational points are located on land areas.

[4] Satellite observations have the advantage of observing gravity waves globally [e.g., *Wu and Waters*, 1996; *Tsuda et al.*, 2000; *Preusse et al.*, 2002; *Ratnam et al.*, 2004; *Randel and Wu*, 2005; *Hei et al.*, 2008]. *Tsuda et al.* [2000] used Global Positioning System radio occultation (GPS RO) data to study the global distribution of wave potential energy (PE) with vertical wavelengths $\leq$ 10 km. They observed seasonal variation in PE with considerable longitudinal variation. Large PE was generally found in tropical regions between 20°N and 20°S, and a clear relationship between wave activity and cumulus convection was demonstrated in the equatorial region [*Ratnam et al.*, 2004].

[5] The relatively small temporal and spatial scales of gravity waves preclude comprehensive investigations of gravity waves over a wide geographic range using only observational data. Atmospheric general circulation models (AGCMs) are effective tools with which to study the characteristics of gravity waves, including global propagation and momentum fluxes [*O'Sullivan and Dunkerton*, 1995; *Hayashi et al.*, 1997; *Sato et al.*, 1999; *Kawatani et al.*, 2003, 2004, 2005; *Watanabe et al.*, 2006, 2008]. *Sato et al.* [1999] examined the characteristics of gravity waves using an aqua planet AGCM with a resolution of T106L53. Their simulated gravity waves showed good agreement with mesosphere-stratosphere-troposphere (MST) radar observations. They also found a new phenomenon by which gravity waves generated around the polar night jet propagating downward. These results indicated that the polar night jet may be one source of gravity waves [*Hei et al.*, 2008]. The existence of these downward-propagating gravity waves was confirmed by radiosonde observations after their simulation [*Yoshiki and Sato*, 2000; *Sato and Yoshiki*, 2008].

[6] *Kawatani et al.* [2003] conducted a simulation using a T106L60-resolution AGCM with realistic boundary conditions and compared the simulated results with GPS RO data. *Tsuda et al.* [2000] noted interesting regions of large PE around the tropical Atlantic ($\sim$0–30°W, 0–10°S). This is a region with little convection or topographic sources of gravity waves. AGCM simulation has also revealed large PE over the Atlantic Ocean. In their AGCM study, *Kawatani et al.* [2003] clarified the mechanism of PE and showed that the diurnal cycle of convection around the Bay of Guinea generated 3D-gravity waves with a period of approximately 24 h; these gravity waves then propagated southwestward across the equator, and large energy was formed over the Atlantic Ocean.

[7] Mean wind distributions and tropospheric cumulus activities are not zonally uniform in equatorial regions. Thus, gravity waves propagating upward into the stratosphere are not zonally uniform [*Bergman and Salby*, 1994]. *Kawatani et al.* [2005] successfully simulated QBO-like oscillation in a T106L60-resolution AGCM without gravity-wave drag parameterization. The vertical resolution was set at 550 m, because several previous studies indicated that high vertical resolution is required to simulate the QBO-like oscillation in an AGCM [*Takahashi*, 1996, 1999; *Hamilton et al.*, 1999, 2001; *Giorgetta et al.*, 2002; *Horinouchi et al.*, 2003]. *Kawatani et al.* [2005] investigated the zonal distribution of gravity waves with periods of $\leq$3 days during the westerly shear phase (i.e., the westerly is situated over an easterly) of the QBO. They demonstrated a nonuniform distribution between the eastern hemisphere and western hemisphere in vertical flux of the zonal momentum ($\overline{u'w'}$) of gravity waves in the upper troposphere because of differences in the vertical shear of the Walker circulation. Large-magnitude upward fluxes with eastward momentum ($\overline{u'w'} > 0$) dominated in the eastern hemisphere, whereas relatively small-magnitude upward fluxes with westward momentum ($\overline{u'w'} < 0$) dominated in the western hemisphere. The wave momentum flux divergence also varied with longitude. As a result, the eastward forcing due to gravity waves in the eastern hemisphere was much greater than that in the western hemisphere at the altitude where the QBO changed from easterly to westerly.

[8] Recently, *Alexander et al.* [2008b] reported the global distribution of PE associated with atmospheric waves in the equatorial upper troposphere and lower stratosphere (UTLS), using temperature profiles derived from GPS RO data from the Constellation Observing System for Meteorology, Ionosphere, and Climate (COSMIC) satellite network. COSMIC GPS RO data have markedly improved temporal and spatial resolutions in comparison to previous GPS RO data. Interestingly, *Alexander et al.* [2008b] reported off-equatorially trapped PE structures that may have been caused by MRG waves. Satellites with low temporal resolutions have observed long-period Kelvin waves, but may not have detected clear EQW signals with relatively short periods. The dominant periods and zonal wavelengths of MRG waves are shorter and smaller than those of Kelvin waves [*Yanai and Maruyama*, 1966; *Wallace and Kousky*, 1968]. In fact, previous analyses using satellite data often focused on Kelvin waves with zonal wave numbers of 1–2. *Alexander et al.* [2008b] extracted the wave components of Kelvin waves and MRG waves with zonal wave numbers $\leq$ 9 and discussed the interactions between these waves and the mean flow. Recently, *Ern et al.* [2008] conducted equatorial wave analysis from Sounding of the Atmosphere using Broadband Emission Radiometry (SABER) temperatures, which had a high resolution of approximately 2 km vertically and covered zonal wave numbers up to 6–7. They illustrated the activities of Kelvin waves, $n = 1$ equatorial Rossby waves, MRG waves, and $n = 0$ eastward-propagating waves in time-height and longitude-time cross-sections. Their results indicated that EQWs with relatively small vertical wavelengths are mainly modulated by the QBO.

[9] High-resolution GPS RO data allow calculation of temperature, but not of wind components. Therefore global propagation direction and momentum fluxes of gravity waves cannot be calculated directly using observational data. In this case, the comparison of satellite observations and AGCM results is useful to understand the global characteristics of atmospheric waves [*Kawatani et al.*, 2003; *Alexander et al.*, 2008a]. *Alexander et al.* [2008a]

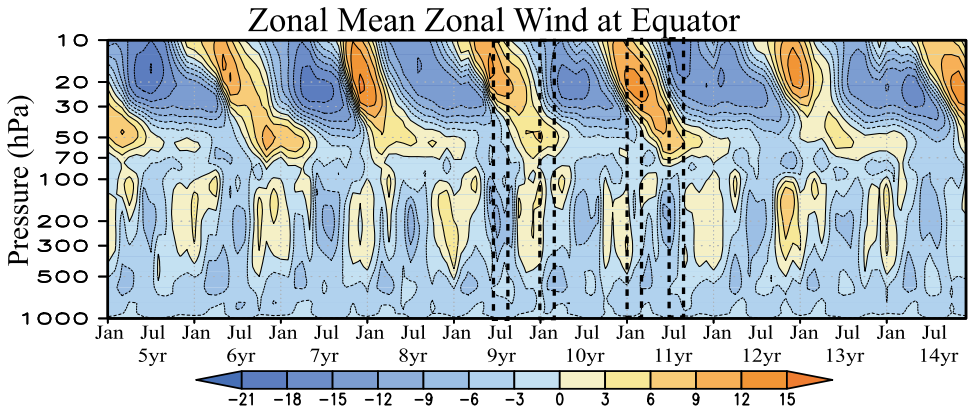

Figure 1. Time-height cross-section of zonal-mean zonal wind at the equator (m s^{-1}). Westerlies (eastward wind) and easterlies (westward wind) are indicated in red and blue, respectively. Boxed areas with dashed lines indicate the periods analyzed.

used COSMIC GPS RO data and analyzed PE with vertical wavelength $\leq$ 7 km during northern winter in 2006–2007. Large PE at 17–23 km associated with the subtropical jet was observed and showed significant longitudinal variability. COSMIC results were compared with those of the T106L60 AGCM, and they concluded that gravity waves generated around the subtropical jet with eastward ground-based zonal phase velocity (Cx) of $\sim$10 m s^{-1} propagated upward, creating large PE around the 0–10 m s^{-1} background westerly (eastward wind) in the stratosphere.

[10] In the present study, we illustrated the global distribution, sources, and propagation of EQWs and 3D-gravity waves simulated by an AGCM and compare the results with recent satellite observations. As the model has sufficient spatial and temporal resolution, EQWs from the $n = -1$ mode (Kelvin waves) to the $n = 2$ mode were investigated. Eastward-propagating and westward-propagating inertia-gravity waves with a mode of $n = 1/n = 2$ are referred to as $n = 1/n = 2$ EIGWs and WIGWs, respectively. For the $n = 0$ mode, eastward and westward-propagating EQWs are referred to as $n = 0$ EIGWs and MRG waves, respectively, as in previous studies [e.g., *Wheeler and Kiladis*, 1999]. We describe the model in section 2. In section 3, we discuss general aspects of the study. In section 4, we describe the global distribution, sources, and propagation of atmospheric waves, which is followed up with summary and concluding remarks in section 5.

2. Model Description

[11] We used the Center for Climate System Research/National Institute for Environmental Studies/Frontier Research Center for Global Change (CCSR/NIES/FRCGC) AGCM [*K-1 Model Developers*, 2004]. The model has T106 truncation, which corresponds to a grid interval of approximately 120 km in the tropics. There are 60 vertical layers (L60), and the top boundary is at 1 hPa ($\sim$50 km). The thickness of the model layers is $\sim$35 m in the lowest part of the troposphere, which increases gradually to 900 m in the middle troposphere, and then decreases to 550 m in the upper troposphere and middle stratosphere. The maximum altitude analyzed in the present study was 32 km (10 hPa) for which a high vertical resolution was set. The cumulus parameterization was based on that reported by *Arakawa and Schubert* [1974]. A relative humidity limit method was incorporated into the cumulus convection scheme [*Emori et al.*, 2001]. If the ratio between the vertical integration of the specific humidity and that of the saturation specific humidity from the bottom to the top of a cloud is less than a critical value (here, 0.7), the cloud mass flux is set to zero (see *Emori et al.* [2001] for further details). The prognostic cloud water was computed using the scheme of *Le Treut and Li* [1991].

[12] The *Mellor and Yamada* [1982] level-2 closure scheme was used for vertical diffusion. A dry convective adjustment was applied to represent wave breaking in the stratosphere. More detailed explanations of vertical diffusion and dry convective adjustments in the AGCM have been provided by *Watanabe et al.* [2008]. This experiment included no gravity-wave drag parameterization. Fourth-order horizontal diffusion with a damping time of 4 days at the maximum wave number reduced numerical noise. Daily sea surface temperature (SST), which was temporally interpolated from the climatology of monthly SSTs, and realistic topography were used as bottom boundary conditions. Other parameterizations and numerical methods matched the standard CCSR/NIES/FRCGC AGCM [*K-1 Model Developers*, 2004]. Gravity waves were investigated using 3-hourly data sampled for four periods in January–February (Jan–Feb) and July–August (Jul–Aug) when the westerly and easterly shear phases of the QBO were obvious, respectively.

3. General Aspects

[13] The model successfully simulated the observed features of the atmospheric general circulation. The position and strength of the subtropical jet were realistic in both hemispheres. The results also indicated realistic separation between the subtropical jet and the polar night jet [*Kawatani et al.*, 2004]. Cumulus convective activity, such as westward-propagating cloud clusters and eastward-propagating super cloud cluster-like structures, were simulated reasonably well as shown by comparison with observations [*Nakazawa*, 1988].

[14] Simulated equatorial winds in the lower stratosphere were also reasonable. Figure 1 shows a time-height cross-

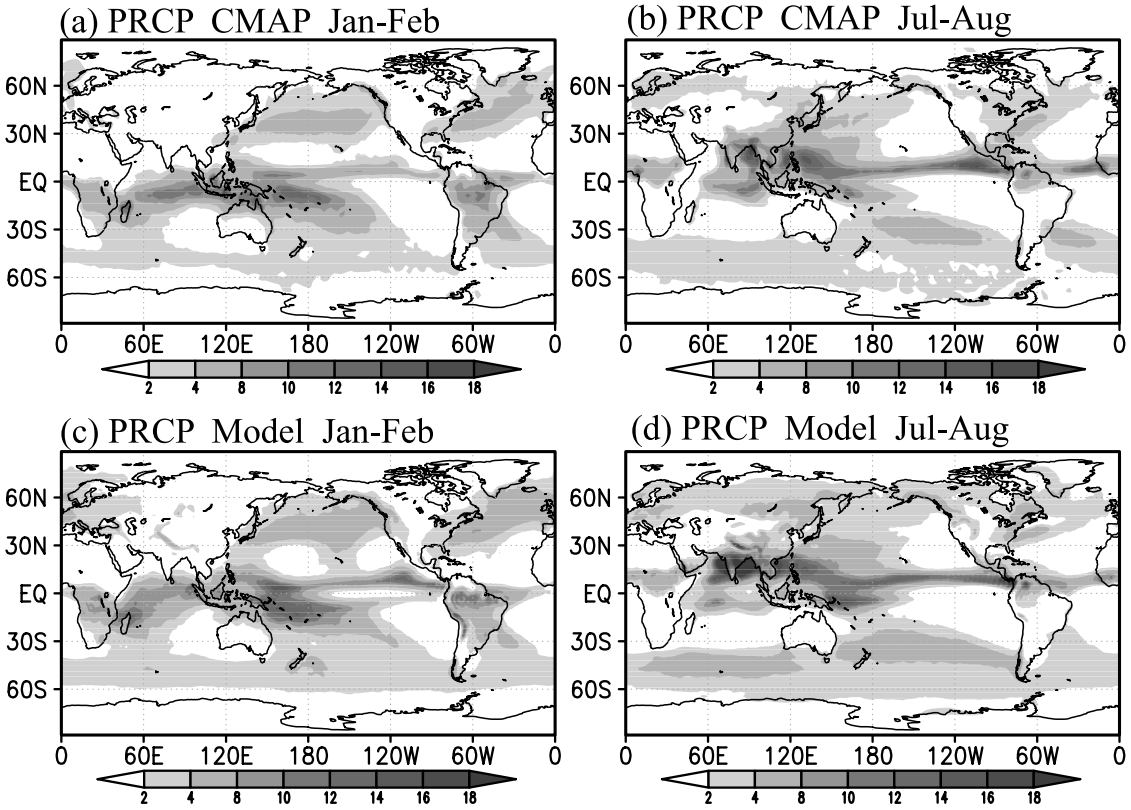

Figure 2. Global distribution of precipitation (mm day^{-1}) in (a, c) Jan–Feb and (b, d) Jul–Aug obtained with (a, b) CMAP and (c, d) the model. The observational values are 26-year averages, whereas the model values are 17-year averages. The shaded interval is 2 mm day^{-1}; values $\geq$ 2 mm day^{-1} are shown.

section of zonal-mean zonal wind along the equator. An obvious QBO-like oscillation has a period of approximately 1.5–2 years. The maximum speed of the easterly (westward wind) was approximately 20 m s^{-1}, and that of the westerly (eastward wind) was 15 m s^{-1}. In contrast, *Naujokat* [1986] reported amplitudes of 35 and 20 m s^{-1} for easterly and westerly winds, respectively. The simulated amplitude of the easterly was larger than that of the westerly, as in the real atmosphere, despite the smaller amplitude of the oscillation. The easterly extends down to approximately 40–50 hPa in the model, which is slightly higher than the observed. The downward propagation of the westerly shear zones of zonal wind ($\partial u/\partial z > 0$, where z denotes altitude) was faster than the downward propagation of easterly shear zones ($\partial u/\partial z < 0$), which agreed with observations. We analyzed four periods when the QBO was in its westerly and easterly shear phases in Jan–Feb and Jul–Aug, respectively, as indicated by the boxed areas in Figure 1. The 0 m s^{-1} zonal winds were at approximately 30 hPa during these periods.

[15] Figure 2 shows the global distribution of precipitation in Jan–Feb and Jul–Aug obtained by observation and in the model. The observation data are Center for Climate Prediction (CPC) Merged Analysis of Precipitation (CMAP; *Xie and Arkin*, 1996) 26-year averaged values (1979–2004). The simulated precipitation is 17-year averaged. The model reasonably simulated the global distribution of precipitation. In Jan–Feb, most large precipitation areas were distributed around or to the south of the equator over the Indian Ocean, whereas in Jul–Aug strong precipitation occurred over the Indian monsoon region in the Northern Hemisphere. Strong precipitation also occurred over Africa and South America in both Jan–Feb and Jul–Aug. The Inter-Tropical Convergence Zone (ITCZ) in the equatorial region was also well simulated. The separation between the ITCZ and the South Pacific Convergence Zone (SPCZ) is clearly illustrated.

[16] To evaluate how well the model simulates convectively coupled EQWs, we performed space-time spectral analysis of precipitation according to the method of *Lin et al.* [2006] using daily data from the Global Precipitation Climatology Project (GPCP) and the model output. The data length for spectral calculation was 2 years. GPCP data from 2004 to 2005 were used when the influence of El Niño or La Niña was small, based on the criteria for those events defined by the Japan Metrological Agency.

[17] Here we present a brief outline of the procedure; further details were provided by *Wheeler and Kiladis* [1999] and *Lin et al.* [2006]. Grid data D(φ) as a function of latitude φ can be expressed as the sum of symmetric DS(φ) and antisymmetric DA(φ) components as follows:

$$\mathrm{D}(\varphi) = \mathrm{DS}(\varphi) + \mathrm{DA}(\varphi) \quad (1)$$

$$\mathrm{DS}(\varphi) = [\mathrm{D}(\varphi) + \mathrm{D}(-\varphi)]/2 \quad (2)$$

$$\mathrm{DA}(\varphi) = [\mathrm{D}(\varphi) - \mathrm{D}(-\varphi)]/2 \quad (3)$$

Precipitation data were decomposed into symmetric and antisymmetric components and averaged from 15°N to

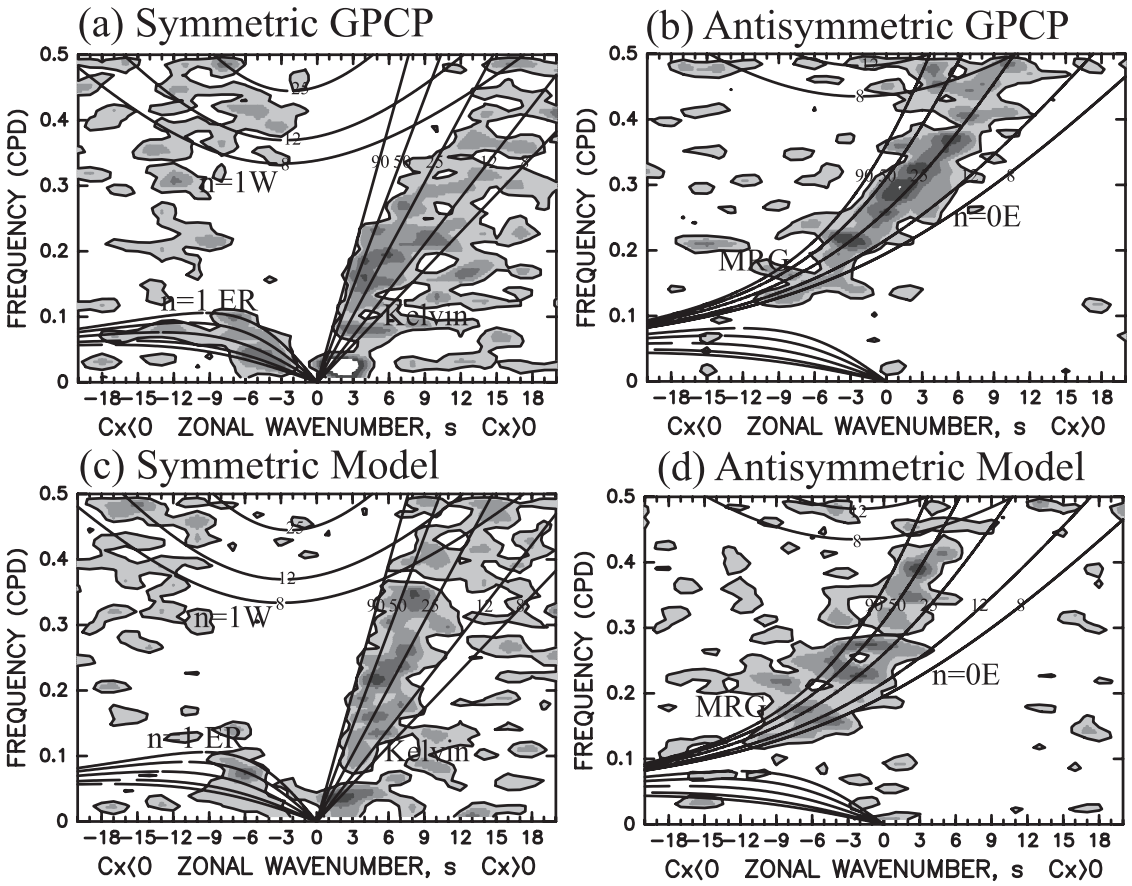

Figure 3. Zonal wave number versus frequency spectra of precipitation averaged from 15°N to 15°S. (a, c) Symmetric and (b, d) antisymmetric components of precipitation divided by the background spectrum appearing in the (a, b) GPCP data and (c, d) the model. Positive (negative) zonal wave number corresponds to positive (negative) Cx. The shading interval is 0.2; values $\geq$ 1.1 are shown. Dispersion curves indicate the odd and even modes of equatorial waves with the five equivalent depths of 8, 12, 25, 50, and 90 m. The frequency spectral width is 1/128 cpd.

15°S. Space-time spectra were then calculated for successive overlapping segments of data and averaged. Here 128 days, with 78 days of overlap between each segment, were calculated. The "background spectra" were calculated by averaging the powers of DA and DS and smoothing with a 1–2–1 filter in frequency and wave number. This smoothing was applied to remove any periodic signals that may be present in the spectra at a particular zonal wave number and frequency.

[18] *Matsuno* [1966] derived the dispersion relation of EQW modes in shallow-water equations on an equatorial beta plane as follows:

$$\frac{m^2\hat{\omega}^2}{N^2} - k^2 - \frac{\beta k}{\hat{\omega}} = (2n+1)\frac{\beta|m|}{N}, \quad n = 0, 1, 2, \ldots \qquad (4)$$

where m, $\hat{\omega}$, N, k, β, and n are the vertical wave number, the intrinsic frequency, the buoyancy frequency, zonal wave number, meridional gradient of the Coriolis parameter, and order of the solution, respectively. The solutions of wave modes have structures trapped at the equator. For an EQW with zero meridional wind components, i.e., Kelvin waves ($n = -1$), the dispersion relation is the same as that for internal gravity waves with zero meridional wavenumber as follows:

$$\frac{\hat{\omega}^2}{k^2} = gh_e \qquad (5)$$

where h_e is equivalent depth, which is connected with the vertical wave number m as follows

$$m^2 = \left(\frac{N^2}{gh_e} - \frac{1}{4H^2}\right) \qquad (6)$$

where H is the scale height, and the vertical wavelength λ_z is calculated from the vertical wave number as $\lambda_z = 2\pi/m$ (see *Andrews et al.* [1987] for detailed derivation of above equations).

[19] Figure 3 shows the zonal wave number versus the frequency spectra of symmetric and antisymmetric components of precipitation divided by the background spectra appearing in the GPCP data and the model (15°S–15°N average). Following *Lin et al.* [2006], powers of 1.1 times the background or greater are drawn. The dispersion curves of the odd ($n = -1$, 1) and even modes ($n = 0$, 2) of

equatorial waves for the five equivalent depths of 8, 12, 25, 50, and 90 m are superposed under the assumption of zero background wind. The frequency spectral width is 1/128 circles per day (cpd). As the time resolution of precipitation is 1 day, the minimum resolvable period is 0.5 cpd (2 days). In the areas corresponding to the dispersion curves, there are clear signals of Kelvin waves, $n = 1$ WIGWs, and $n = 1$ equatorial Rossby waves in symmetric components, whereas MRG waves and $n = 0$ EIGWs are obvious in antisymmetric components, in both the observation and model results.

[20] *Lin et al.* [2006] evaluated the tropical variability of precipitation data in 14 atmosphere-ocean coupled GCMs participating in the Intergovernmental Panel on Climate Change (IPCC) Fourth, Assessment Report (AR4). They reported that the Model for Interdisciplinary Research on Climate (MIROC; the CCSR/NIES/FRCGC AGCM used here is an atmospheric part of MIROC) most realistically simulated power at periods of $\leq$6 days among the 14 models. As shown in their Figures 5–7, MIROC showed good results in simulating convectively coupled equatorial waves. It was also confirmed that spectral values of both symmetric and antisymmetric components are relatively quantitatively well simulated (not shown). Like other AGCMs [cf. *Lin et al.*, 2006], the AGCM used here generally underestimates signals of the Madden-Julian oscillation (MJO [*Madden and Julian*, 1971]). However, analysis of momentum flux indicated that disturbances associated with the MJO did not contribute to driving the simulated QBO (not shown).

[21] *Horinouchi et al.* [2003] conducted a comprehensive comparison of low-latitude middle atmospheric waves using nine AGCMs and showed that the variability of the precipitation spectrum differed greatly among the models. The wave spectrum in the middle atmosphere is linked to the variability of convective precipitation, which is determined by cumulus parameterization. The well-simulated spectrum of precipitation in this study would result in better simulation of equatorial wave activity in the stratosphere.

4. Global Distribution, Sources, and Propagation of Atmospheric Waves

4.1. Waves With Vertical Wavelengths $\leq$ 7 km

[22] PE due to short vertical wavelengths is often used as an indicator of the global distribution of gravity waves (i.e., EQWs and/or 3D-gravity waves) in studies based on GPS RO because PE can be calculated from observed temperature alone. *Alexander et al.* [2008b] reported the global distribution of PE with vertical wavelengths $\leq$ 7 km (PE $\leq$ 7 km). For comparison with their recently obtained results, we also calculated PE $\leq$ 7 km, with PE given by

$$PE = \frac{1}{2}\left(\frac{g}{N}\right)^2 \overline{\left(\frac{T'}{\overline{T}}\right)^2} \tag{7}$$

Here we briefly explain the procedure for extracting short vertical wavelengths of temperature. First, the background temperature profile of $\overline{T}$ was defined by the 2-month average at each grid point. The background temperature $\overline{T}$ was then subtracted from the temperature T of an individual profile, and the linear trend was removed. Next, a cosine-type window was applied to both ends of the data to reduce spectral leakage, and a high-pass filter using fast Fourier transform (FFT) with a cut-off vertical wavelength of approximately 7 km was applied to obtain T' with vertical wavelengths $\leq$ 7 km. The analyzed height ranges in this study do not contain the altitude where the window was applied.

[23] *Alexander et al.* [2008b] binned COSMIC data into horizontal grid cells of 20° × 5° to secure a sufficient number of data points before calculating PE, which allows for the study of waves with zonal wave number $\leq$ 9. In the AGCM, PE is calculated every 3 h using 2-month averaged background temperature $\overline{T}$ at each grid point; these values are then averaged for 2 months in each of the four terms illustrated in Figure 1. Therefore the simulated PE consists of waves with periods from approximately 6 h to 2 months, vertical wavelengths $\leq$ 7 km, and horizontal wavelengths of $\sim$380 to 40,000 km at the equator. Therefore the simulated waves have much wider spectral ranges than those shown by COSMIC data, and the value of simulated PE $\leq$ 7 km should be larger than that observed by COSMIC GPS RO.

[24] Figure 4 shows longitude-height cross-sections of PE $\leq$ 7 km averaged from 10°N to 10°S for the four terms examined (2-month averages), during which the QBO was in westerly and easterly shear phases in Jan–Feb and Jul–Aug. Contour lines show the zonal wind. The zonal distribution of zonal wind was well simulated despite the slightly larger amplitude of the Walker circulation as compared with that in the real atmosphere. The longitudinal variation in outgoing long-wave radiation (OLR) averaged from 10°N to 10°S is shown below each figure. Low values of OLR (note that the vertical axis of the OLR is inverted) correspond to active cumulus convection. The convective activity is large over the Indian Ocean to mid-Pacific and at approximately 60–80°W. In the UTLS region, much larger PE elongates from east to west over the eastern hemisphere than in the western hemisphere, which is consistent with the COSMIC results. Larger PE is also distributed in the eastern hemisphere around the altitude where the zonal wind changes from easterly to westerly at approximately 30 hPa (Figures 4a and 4c), which was also observed in the COSMIC GPS RO data. Simulated PE ranging from 8 to 10 J kg^{-1} was observed at approximately 60–80°W in the UTLS region for all four terms, where a secondary maximum of convective activity occurs. The values of PE $\leq$ 7 km in this simulation were larger than those calculated using the COSMIC data, resulting from the much wider spectral ranges covered in the AGCM. A quantitative comparison is presented in section 4.3.

[25] To clarify which phase velocities of waves are dominant, PE as a function of zonal phase velocity relative to the ground (Cx) was calculated. Figure 5 shows the height distribution of PE $\leq$ 7 km as a function of Cx averaged from 10°N to 10°S for the four terms, which are shown separately as averages in the eastern hemisphere (0–180°E) and western hemisphere (0–180°W). The sign of zonal wind associated with the Walker circulation changes at approximately $\sim$180°E (Figure 4). The 2-month mean vertical profiles of zonal wind with vertical wavelengths > 7 km (i.e., background zonal wind for waves with vertical wavelengths $\leq$ 7 km) averaged in the eastern hemisphere/

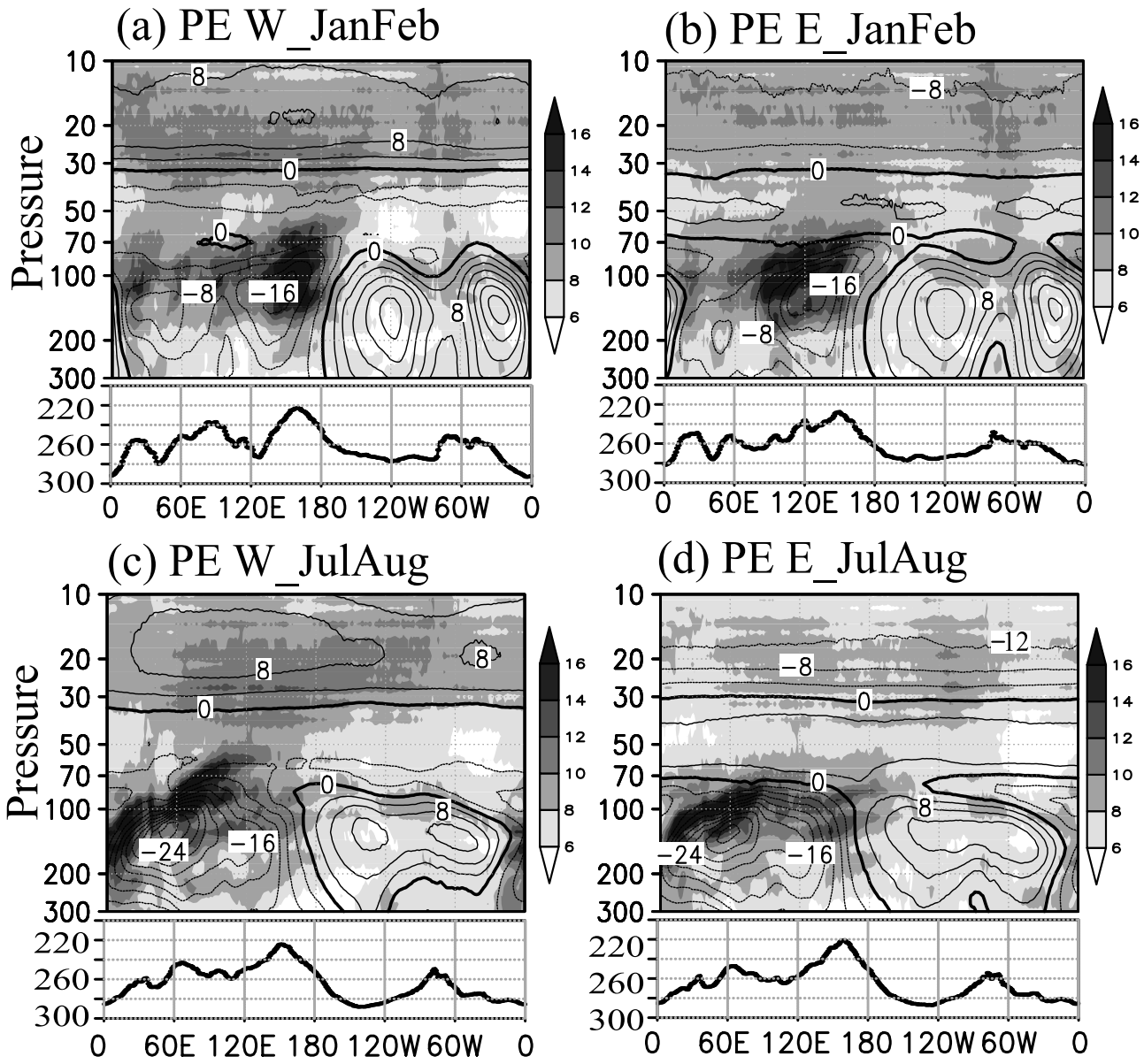

Figure 4. Longitude-height cross-section of PE (shaded) due to waves with vertical wavelengths ≤ 7 km and zonal wind (contour lines). (a, c) Westerly and (b, d) easterly shear phases of the QBO in (a, b) Jan–Feb and (c, d) Jul–Aug. The shading and contour intervals are 2 J kg^{-1} and 4 m s^{-1}, respectively. The line graph indicates the zonal variation in 2-monthly mean OLR (W m^{-2}). Note that the vertical axis of the OLR is inverted. These values are averaged from 10°N to 10°S.

western hemisphere and 10°S–10°N are shown by thick solid lines. The background zonal wind changes in longitude, latitude, and time direction must influence the local propagation of waves. The two dashed lines show the averaged zonal winds plus/minus their standard deviations (i.e., root mean square of longitude, latitude, and time variance of the zonal wind). Note that some stratospheric PE in the western hemisphere (eastern hemisphere) originates from waves generated in the troposphere in the eastern hemisphere (western hemisphere) and then enters the western hemisphere (eastern hemisphere). However, these wave propagations do not critically alter the features mentioned below (zonal propagations of EQWs are shown in Figures 10 and 11).

[26] In the eastern hemisphere (left panels), the easterly (westward wind) associated with the Walker circulation allows most of the eastward waves to propagate from the upper troposphere to the stratosphere, whereas most of the westward-propagating waves with Cx of approximately -10 m s^{-1} are prevented from entering the stratosphere (some westward waves with Cx of ~ -10 m s^{-1} could propagate upward because of local changes in the zonal wind; see the width of the standard deviation). The situation is reversed in the western hemisphere. Most westward-propagating waves are not influenced by the westerly (eastward wind) in the upper troposphere.

[27] In addition to differences in the zonal wind profiles in the troposphere, the wave sources (cumulus convection)

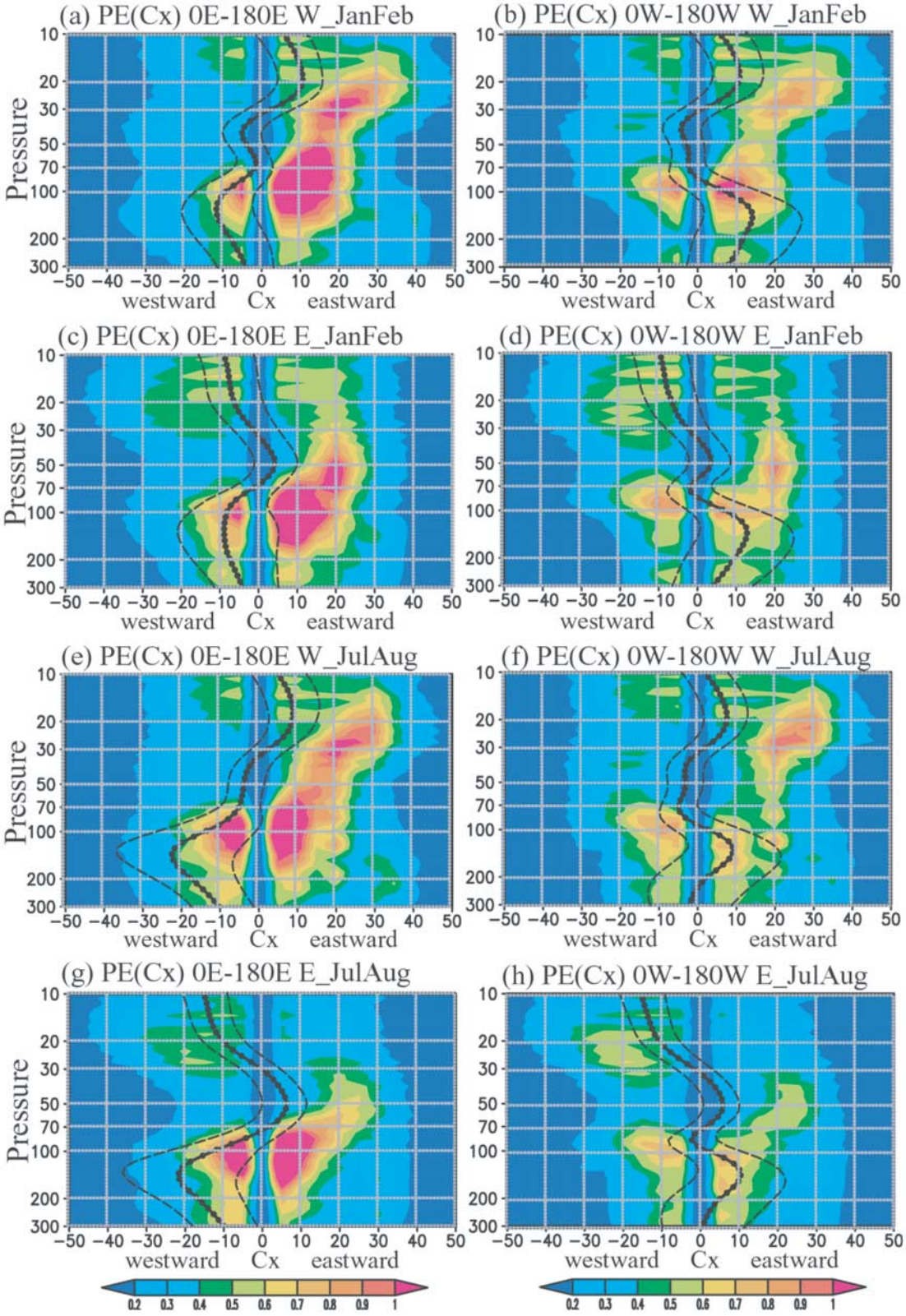

Figure 5. Height distributions of PE $\leq$ 7 km as a function of zonal phase velocity (Cx) in the (left) eastern (0–180°E) and (right) western (0–180°W) hemispheres (10°S–10°N average). (a, b, e, f) Westerly and (c, d, g, h) easterly shear phases of the QBO in (a–d) Jan–Feb and (e–h) Jul–Aug. The shading interval is 0.1 J Kg^{-1} m^{-1} s. The 2-month mean vertical profiles of zonal wind with vertical wavelengths > 7 km averaged zonally in the (left) eastern hemisphere and (right) western hemisphere and meridionally from 10°S–10°N are indicated by thick solid lines; the two dashed lines indicate averaged zonal wind plus/minus the standard deviation. See text for details.

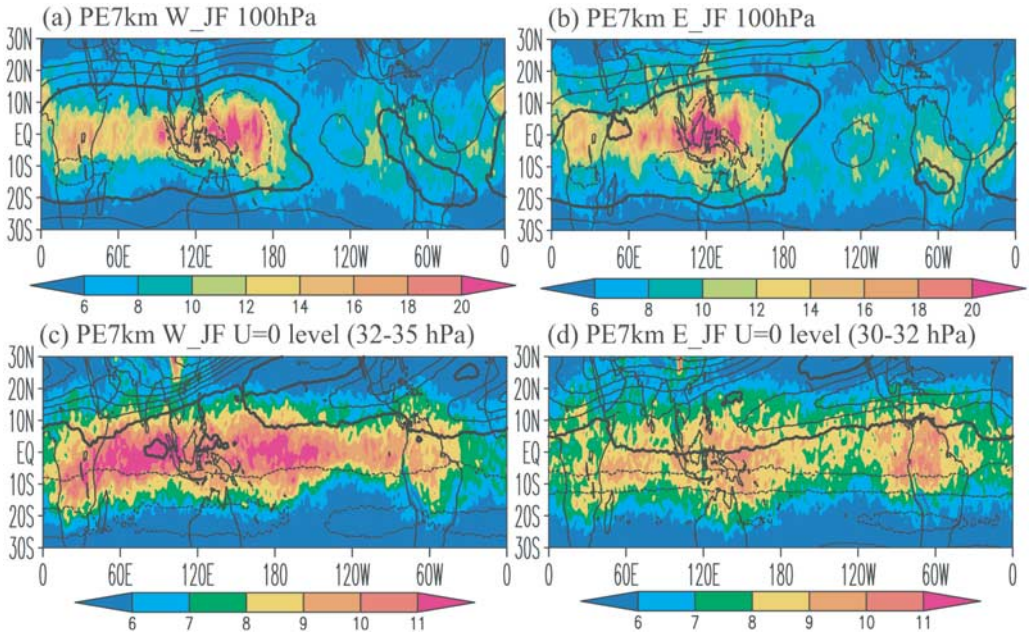

Figure 6. Global distribution of PE $\leq$ 7 km in Jan–Feb at (a, b) 100 hPa, and (c) 32–35 hPa and (d) 30–32 hPa where zonal wind (contour lines) is approximately 0 m s^{-1} at the equator. (a, c) Westerly and (b, d) easterly shear phases of the QBO. The shading interval is 2 J kg^{-1} for (a, b) and 1 J kg^{-1} for (c, d). The solid and dashed lines illustrate westerly and easterly, and thick solid lines show 0 m s^{-1}. The contour interval is 10 m s^{-1}.

are generally larger in the eastern hemisphere than in the western hemisphere, which could result in larger PE in the eastern hemisphere than in the western hemisphere in the UTLS region (Figure 4). PE generally shows large values around the tropopause, which might partially result from a sharp cold point tropopause in the tropical regions [*Alexander et al.*, 2008b]. In addition, the wave energy accumulation might occur around the tropopause because the vertical group velocity is inversely proportional to buoyancy frequency if the zonal wind does not change vertically [*Andrews et al.*, 1987].

[28] In the stratosphere, waves are markedly influenced by the phase of the QBO. In the westerly shear phase of the QBO in the eastern hemisphere (Figures 5a and 5e), the dominant Cx of waves is $\sim$10 m s^{-1} from 200 to 50 hPa, but changes to $\sim$20 m s^{-1} at approximately 30 hPa. Eastward-propagating waves generated in the eastern hemisphere do not encounter the zonal wind until $\sim$30 hPa. Therefore most of the eastward waves can exist until 30 hPa. On the other hand, in the westerly shear phase of the QBO in the western hemisphere (Figures 5b and 5f), isolated large PE occurs at approximately 20–30 hPa with Cx of $\sim$20 m s^{-1}. These Cx values are larger than those of the mean westerly associated with the Walker circulation in the upper troposphere (note also that some PE at this altitude originates from waves generated in the eastern hemisphere, as mentioned above). In the easterly shear phase of the QBO (Figures 5c, 5d, 5g, and 5h), PE with Cx of approximately -10 m s^{-1} is generally larger than that with Cx of approximately 10 m s^{-1} over 20–30 hPa. The PE distribution in the stratosphere generally agrees with the fact that temperature variances associated with zonally and vertically propagating gravity waves in background shear flow have a functional dependence of $|\overline{u} - \mathrm{Cx}|^{-1}$, where $\overline{u}$ is background zonal wind. Nonlinear effects and dissipation would limit the growth close to the critical level, so that temperature variances maximize below [*Randel and Wu*, 2005 and references therein]. The results obtained from Figures 4 and 5 indicate that the distribution of the PE results from three factors: the source strengths, the Walker circulation, and the phase of the QBO.

[29] *Alexander et al.* [2008b] showed the global distribution of PE $\leq$ 7 km at 15, 22, 26, and 32 km in January 2007 and 2008, when the QBO was in its easterly and westerly shear phases, respectively. For both 2007 and 2008, they found similar PE distributions at 15 km, as well as similar OLR distributions. Large PE is visible from the Indian Ocean through the Western Pacific and over South America. However, the stratospheric PE is different between the different phases of the QBO. Around the altitude where the zonal wind is $\sim$0 m s^{-1}, relatively large PE elongates more zonally in the westerly than in the easterly shear phase of the QBO. Another interesting point is that large PE is found over South America in both the easterly and westerly shear phases of the QBO.

[30] Figure 6 shows the global distribution of PE in Jan–Feb at 100 hPa (Figures 6a and 6b) and the altitude at which zonal wind is approximately 0 m s^{-1} at the equator in the westerly (approximately 32–35 hPa; Figure 6c) and easterly (approximately 30–32 hPa; Figure 6d) shear phases of the QBO. The PE distributions at 100 hPa do not differ much between the two phases; large PE is observed mainly from the Indian Ocean to the western Pacific, and PE of approximately 8–16 J kg^{-1} is located over South America, the eastern Pacific, and the Congo Basin. These results are qualitatively similar to those observed by COSMIC. The PE

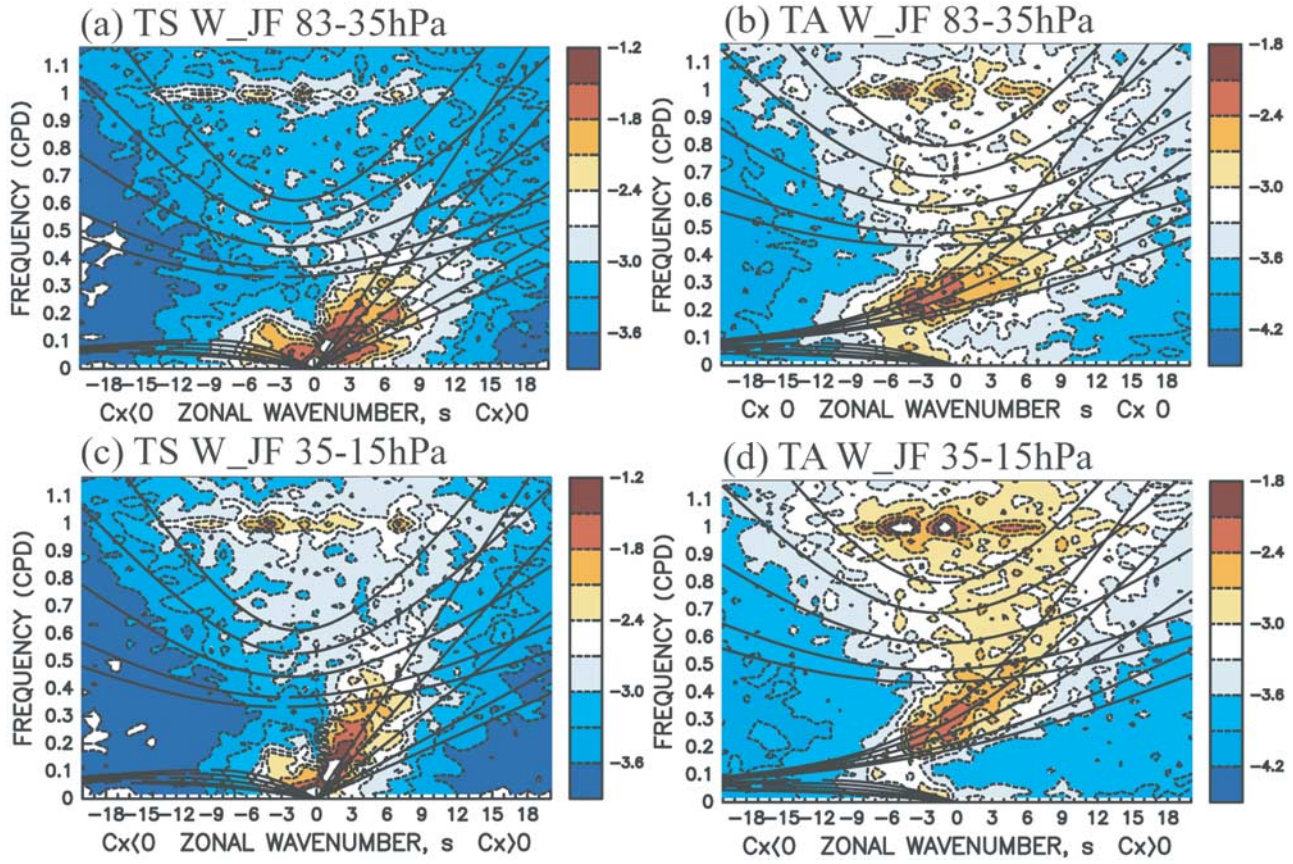

Figure 7. Zonal wave number versus the frequency spectra of the (a, c) symmetric and (b, d) antisymmetric components of temperature for the westerly shear phase in Jan–Feb at (a, b) 83–35 hPa and (c, d) 35–15 hPa. Spectral units are $\log_{10}(K^2$ wave number^{-1} cpd$^{-1})$. Dispersion curves for symmetric components include Kelvin waves, n = 1 EIGWs and WIGWs, and n = 1 equatorial Rossby waves, whereas antisymmetric components include MRG waves, n = 0 EIGWs, n = 2 EIGWs and WIGWs, and n = 2 equatorial Rossby waves. Equivalent depths are selected as 8, 12, 25, 50, and 90 m, which are the same as in Figure 3. The effect of background wind is neglected to draw the dispersion curves of the equatorial waves. Note that the ranges of shading are different between the symmetric and antisymmetric components. Smoothing was conducted with a 1-2-1 moving mean in frequency.

distribution is quite different between the westerly and easterly shear phases of the QBO for which zonal wind is $\sim$0 m s^{-1} (Figures 6c and 6d). Zonally elongating PE with large values occurs from 10–330°E (30°W) above the equator in the westerly shear phase. During the easterly shear phase, relatively small values of PE elongate around the equator and are more scattered than those in the westerly shear phase. Large PE is observed over South America in both the westerly and easterly shear phases. The illustrated PE consists of both EQWs and 3D-gravity waves. The PE with a meridional symmetric mode may be due to EQWs, whereas that scattered in the latitudinal direction is probably due to 3D-gravity waves, as discussed in section 4.3.

4.2. Equatorial Trapped Waves

[31] To investigate what kind of EQWs appear in the model, Figure 7 shows the zonal wave number versus the frequency spectra of the symmetric and antisymmetric components of temperature for the westerly shear phase in Jan–Feb. Spectra of symmetric and antisymmetric components were computed separately for each latitude before averaging from the equator to 10° (i.e., equivalent to the average of 10°S–10°N). Note that temperature data were nonfiltered in both space and time before calculation of the spectra (i.e., the vertical wavelength filter used in section 4.1 was not applied). In the stratospheric temperatures, the spectrum is not the red noise-like background spectrum dominating in OLR data or precipitation data [e.g., *Wheeler and Kiladis*, 1999]. Therefore symmetric and antisymmetric spectra were not divided by the background spectra.

[32] The altitude ranges were selected from 83–35 hPa and 35–15 hPa. The boundary of 35 hPa corresponds roughly to the altitude at which the zonal wind changes from easterly to westerly. Dispersion curves for symmetric components include Kelvin waves, n = 1 EIGWs and WIGWs, and n = 1 equatorial Rossby waves, whereas antisymmetric components include MRG waves, n = 0 EIGWs, n = 2 EIGWs and WIGWs, and n = 2 equatorial Rossby waves. Equivalent depths were selected as 8, 12, 25, 50, and 90 m, as in Figure 3 (note that the frequency range was extended to $\sim$1.1 cpd because 3-hourly data were used to calculate the spectra). The effect of background wind was neglected when drawing the dispersion curves of the equatorial waves.

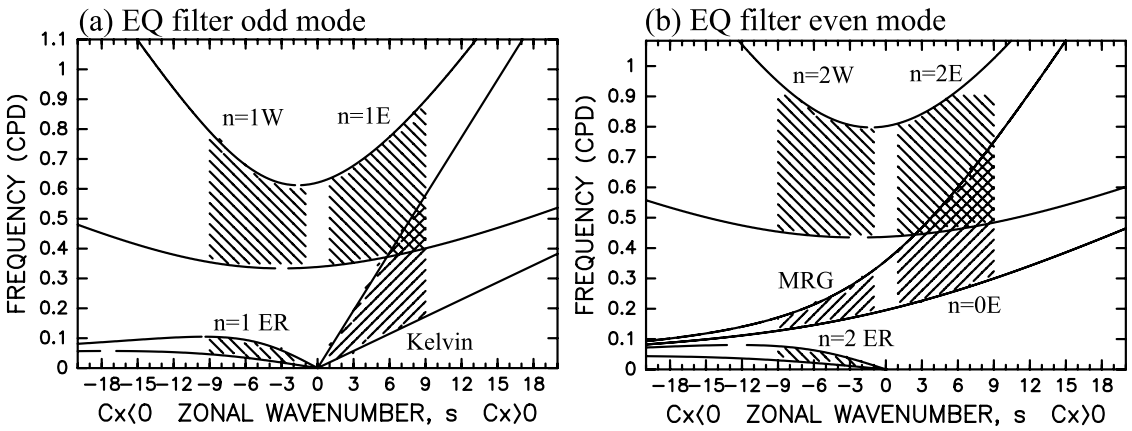

Figure 8. Equatorial wave filter for (a) odd and (b) even modes. Superposed are the dispersion curves of each EQW for two equivalent depths of 8 and 90 m. Hatched areas between the two lines are the filtering range of (a) Kelvin, $n = 1$ EIGWs and WIGWs, $n = 1$ equatorial Rossby waves, (b) MRG waves, $n = 0$ EIGWs, $n = 2$ EIGWs and WIGWs, and $n = 2$ equatorial Rossby waves. The minimum period is set at 1.1 day (~0.9 cpd) to avoid including waves with a period of 1 day. Some overlapping areas occur between the Kelvin waves and $n = 1$ EIGWs and between $n = 0$ and $n = 2$ EIGWs.

[33] For zonally propagating waves, the intrinsic frequency $\hat{\omega}$ is written as follows:

$$\hat{\omega} = \omega - k\overline{u} \tag{8}$$

where ω, k, and $\overline{u}$ are the ground-based frequency, zonal wave number, and background zonal wind, respectively. The intrinsic frequencies $\hat{\omega}$ and vertical wavelengths change because $\overline{u}$ changes with altitude. On the other hand, the ground-based frequency ω of a wave is defined at the wave source level. Note that the ground-based frequency ω and zonal wave number k do not change with altitude, assuming a slowly varying background wind field, even through the background wind changes with altitude; the distribution of the zonal wave number versus the frequency spectra is independent of altitude. The distribution of the spectra would be changed only if a wave were to undergo critical level filtering and/or wave dissipation. Therefore in Figure 7 we selected the same dispersion curves of EQWs as those of the sources (Figure 3) to compare spectral features in the stratosphere with those of the sources. A more detailed discussion was presented by *Ern et al.* [2008, and references therein]. We did not use a vertical wavelength filter to preserve this wave property.

[34] Clear signals of Kelvin waves, MRG waves, $n = 0$ EIGWs, and $n = 1$ equatorial Rossby waves can be seen in Figure 7. The peaks corresponding to $n = 1$ EIGWs became much clearer when the same spectral figures were drawn using meridional wind data in which Kelvin waves do not appear (not shown). Note that the spectral distributions of the temperature at 83–35 hPa (Figures 7a and 7b) were relatively similar to those of precipitation (Figure 3) in the range of $8 \leq h_e \leq 90$ m. These results imply a connection between stratospheric EQWs and tropospheric wave sources of convectively coupled EQWs. On the other hand, the wave spectrum also shows distributions outside the h_e of 8–90 m, especially at 35–15 hPa (Figures 7c and 7d), which are likely independent of convectively coupled EQWs. Waves with large equivalent depth could be an indication of processes involving longer vertical scales in the troposphere, which become visible at higher altitudes due to a decrease of atmospheric density and an increase in statistic stability [*Ern et al.*, 2008]. The powers of Kelvin waves and $n = 0$ EIGWs with small equivalent depths ($h_e \sim 8$ m) decreased with height, implying that these waves interact with the mean zonal wind. There are other spectral peaks with periods of approximately 1 day and a wide zonal wave number range in both symmetric and antisymmetric components. These wave numbers may correspond to the tide and 3D-gravity waves generated by the diurnal cycle of convection [*Kawatani et al.*, 2003].

[35] To investigate the global distribution, sources, and propagation of EQWs, an equatorial wave filter was constructed. Kelvin waves, MRG waves, $n = 0$ EIGWs, $n = 1$ and $n = 2$ EIGWs and WIGWs, and $n = 1$ and $n = 2$ equatorial Rossby waves were extracted separately for further examination according to the methods of *Wheeler and Kiladis* [1999]. To avoid degradation of the actual amplitude of EQWs during the analyzed periods, we included data from both before and after each analyzed period. For example, when the EQWs in January–February were extracted, the last few days of December and the first few days of March were included. Then, a cosine-type window was applied only to the data from December and March. After applying FFT to the combined data, only the data from 1 January to the end of February were extracted.

[36] Figure 8 shows the spectral ranges between the lines indicating equivalent depths of 8 and 90 m under the assumption of zero background wind in the zonal wave number-frequency domain for odd and even modes. The equivalent depths of 8 to 90 m correspond to vertical wavelengths of 2.3 and 7.6 km with $N^2 = 6 \times 10^{-4}$ s^{-2}, which is the representative value in the lower stratosphere (~80 hPa). The vertical wavelength range is similar to that used in the PE calculation in Figures 4–6. The zonal wave numbers of the EQWs were selected from 1 to 9 according to the method of *Alexander et al.* [2008b]; this range corresponds to zonal wavelengths from 4444 to 40,000 km

over the equator. The minimum period was set at 1.1 day (~0.9 cpd) to avoid including waves with a period of 1 day.

[37] *Ern et al.* [2008] reported that EQW activity in a slow phase speed wave band between equivalent depths of 8 and 90 m was mainly modulated by the QBO and that higher equivalent depths (90–2000 m) showed less pronounced variation due to the QBO but more variation due to the stratopause SAO. As we could analyze data up to approximately 32 km in this model, we focused on wave activity related to the QBO. Therefore the selected wave band was set between 8 and 90 m.

[38] In this section, we describe application of the equatorial wave filter to unfiltered data (i.e., original data with no temporal or spatial filtering). The propagation properties of EQWs in relation to background winds from the troposphere to the stratosphere can be investigated using this filter since the ground-based frequency ω and zonal wave number k of a wave do not change unless a wave has dissipated, as mentioned above. The spectral range of $n = 1$ EIGWs may include some fast Kelvin waves ($h_e > 90$ m) with periods of less than ~3 days (see Figures 7a, 7c, and 8a). However, most fast Kelvin waves do not exist in the filtering range of $n = 1$ EIGWs. In fact, fast Kelvin waves have periods of approximately 6–10 days [*Hirota*, 1978; *Hitchman and Leovy*, 1988]. Ultra-fast Kelvin waves with periods of 3–4 days [*Salby et al.*, 1984] are dominant at much higher altitudes than those examined here. There are some areas of overlap between the Kelvin waves and $n = 1$ EIGWs, and between $n = 0$ and $n = 2$ EIGWs.

[39] The amplitudes of the extracted wave component in temperature associated with Kelvin waves and MRG waves are ~2–3 K and ~1 K, respectively. These results were consistent with those from COSMIC GPS RO data [*Alexander et al.*, 2008b] and SABER data [*Ern et al.*, 2008]. We confirmed that the period, zonal phase speed relative to the ground, and vertical wavelength were also simulated realistically in the model. Not only temperature, but also the zonal and meridional wind and geopotential height of EQW components, were extracted using the equatorial wave filter. In addition, we confirmed that the spatial structures of extracted EQWs in the stratosphere agreed with those derived theoretically by *Matsuno* [1966].

[40] To investigate source distributions of these EQWs, the equatorial wave filter was also applied for OLR data. The spectral characteristics of the zonal wave number versus the frequency spectra of OLR (not shown) are similar to those of precipitation shown in Figure 3. Signals of convectively coupled EQWs that appeared in OLR data were extracted using the same equatorial wave filter shown in Figure 8. Therefore we can investigate the wave source distributions, propagations, and global distributions of EQWs.

[41] Figure 9 illustrates the global distribution of OLR variance due to each convectively coupled EQW component and the PE associated with each EQW at 32–35 hPa in Jan–Feb during the westerly shear phase of the QBO. The variances of equatorial Rossby waves with equivalent depths of 8–90 m are much larger in the upper troposphere than in the stratosphere. The connection of the equatorial Rossby waves between the upper troposphere and stratosphere is not very clear (not shown). The vertically propagating responses of convectively coupled $n = 1$ equatorial Rossby waves are confined to within a few kilometers of the wave forcing (see discussions by *Wheeler et al.*, 2000 and references therein). Therefore EQWs without equatorial Rossby waves are discussed in this section. *Wheeler et al.* [2000] reported the global distributions of OLR variance due to each EQW for northern/southern summer using data for a period of ~17 years (see their Figure 3). They also presented the temporal variation of OLR variance for each EQW. Our results shown in Figure 9 are from 2-month averaged fields, and the range of the equatorial wave filter is slightly different from that used by *Wheeler et al.* [2000]. Therefore it is not necessary for the model results to be identical to the observational climatological results. Nevertheless, the distributions of simulated OLR variances are similar to those observed, and the simulated variance of EQWs is in the range of the time variation of observed OLR variance.

[42] *Wheeler et al.* [2000] reported that waves of relatively short vertical wavelength (≤10 km) are indeed important for the coupling of large-scale dynamics and convection. Therefore the global distributions of PE due to EQWs shown in Figure 9 may be related to the activity of convectively coupled OLR. Convectively coupled EQWs would be a sufficient condition for the generation of EQWs propagating into the stratosphere. Concerning MRG waves, *Magaña and Yanai* [1995] discussed that extratropical wave propagating into the tropical region is another possible source of MRG waves. In general, large PE associated with EQWs is observed from the equator to 10°N–10°S. For Kelvin waves, large PE in the stratosphere (Figure 9b) is generally located to the east of source distributions (Figure 9a), suggesting that Kelvin waves generated in the upper troposphere propagate eastward. In contrast, larger PE of $n = 0$ EIGW (Figure 9f) occurs over the Indian Ocean despite larger variance in OLR (Figure 9e) in the Pacific than in the Indian Ocean. It was also interesting that the distributions of large PE with MRG waves and other EQWs do not correspond directly with those of the large variance in OLR.

[43] EQWs propagate eastward or westward from the source region and should be influenced by the background zonal wind. To investigate the propagation of EQWs, 2-month averages of zonal and vertical energy fluxes ($\overline{\phi' u'}$, $\overline{\phi' w'}$) (overbars denote the 2-month average) were used. The ratio of energy flux to energy density is equivalent to the ratio of wave action flux to wave action density when Wentzel-Kramers-Brillouin (WKB) theory holds in space and time. A number of previous studies have provided detailed discussions of wave action flux and wave action density [*Dunkerton*, 1983; *Andrews et al.*, 1987, and reference therein]. The direction of wave group propagation is expressed by energy flux $\boldsymbol{F}$ to energy density E as follows [cf. *Gill*, 1982]:

$$\mathbf{F} = \left(\overline{\phi' u'}, \overline{\phi' w'}\right) = E\left(\hat{C}gx, \hat{C}gz\right) \tag{9}$$

$$E = 1/2\left(\overline{u'^2} + \overline{v'^2} + \overline{w'^2}\right) + 1/2(g/N)^2\overline{\left(T'/\overline{T}\right)^2} \tag{10}$$

where E is wave energy (kinetic energy plus potential energy) per unit mass, and $\hat{C}gx$ and $\hat{C}gz$ represent zonal and

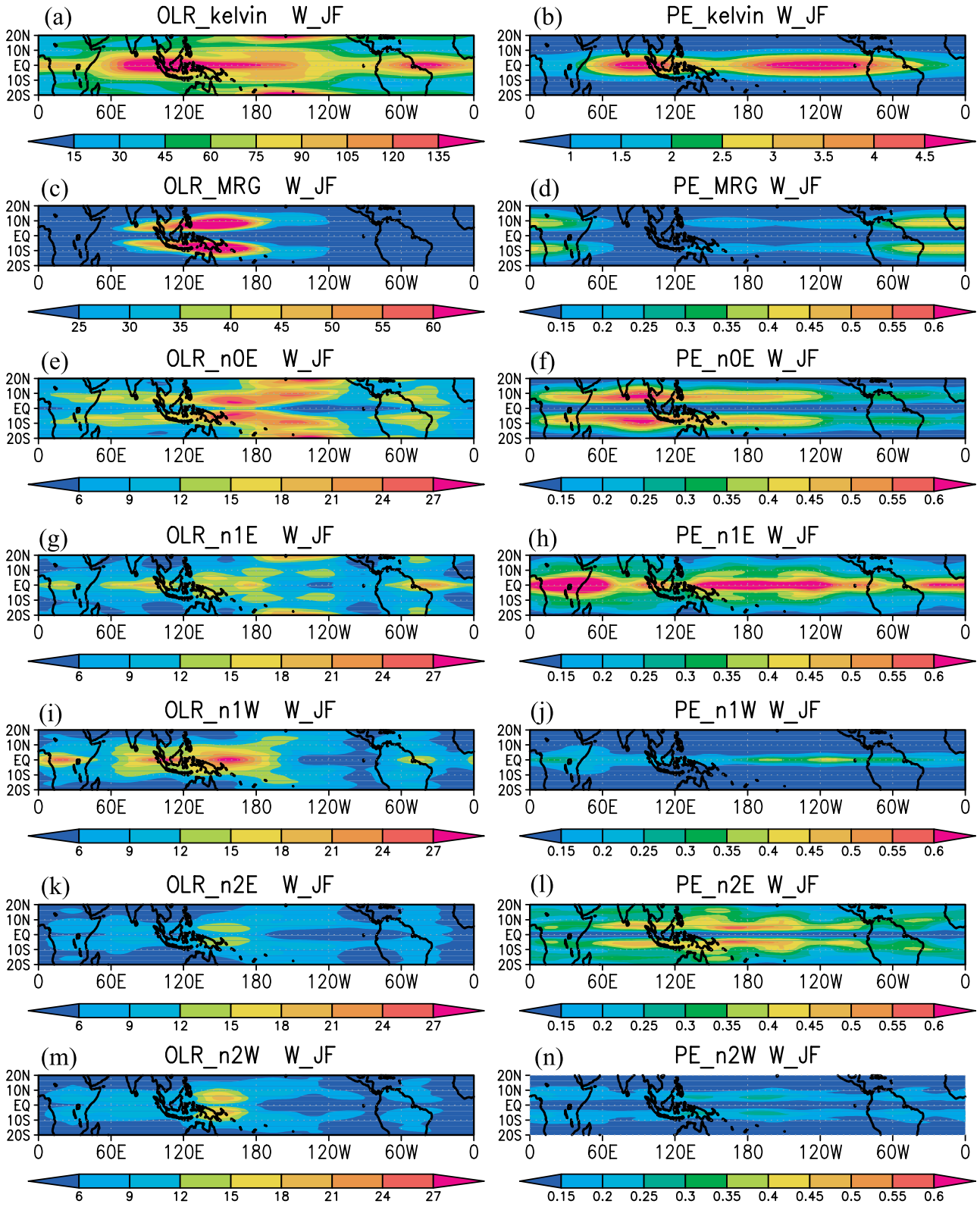

Figure 9. Global distribution of (left) OLR variance due to each convectively coupled EQW component and (right) PE due to each EQW at 32–35 hPa in Jan–Feb during the westerly shear phase of the QBO. (a, b) Kelvin waves, (c, d) MRG waves, (e, f) $n = 0$ EIGWs, (g, h) $n = 1$ EIGWs, (i, j) $n = 1$ WIGWs, (k, l) $n = 2$ EIGWs, and (m, n) $n = 2$ WIGWs. The shading intervals are 15 W^2 m^{-4} for (a), 5 W^2 m^{-4} for (c), 3 W^2 m^{-4} for (e, g, i, k, m), 0.5 J kg^{-1} for (b), and 0.05 J kg^{-1} for (d, f, h, j, l, n).

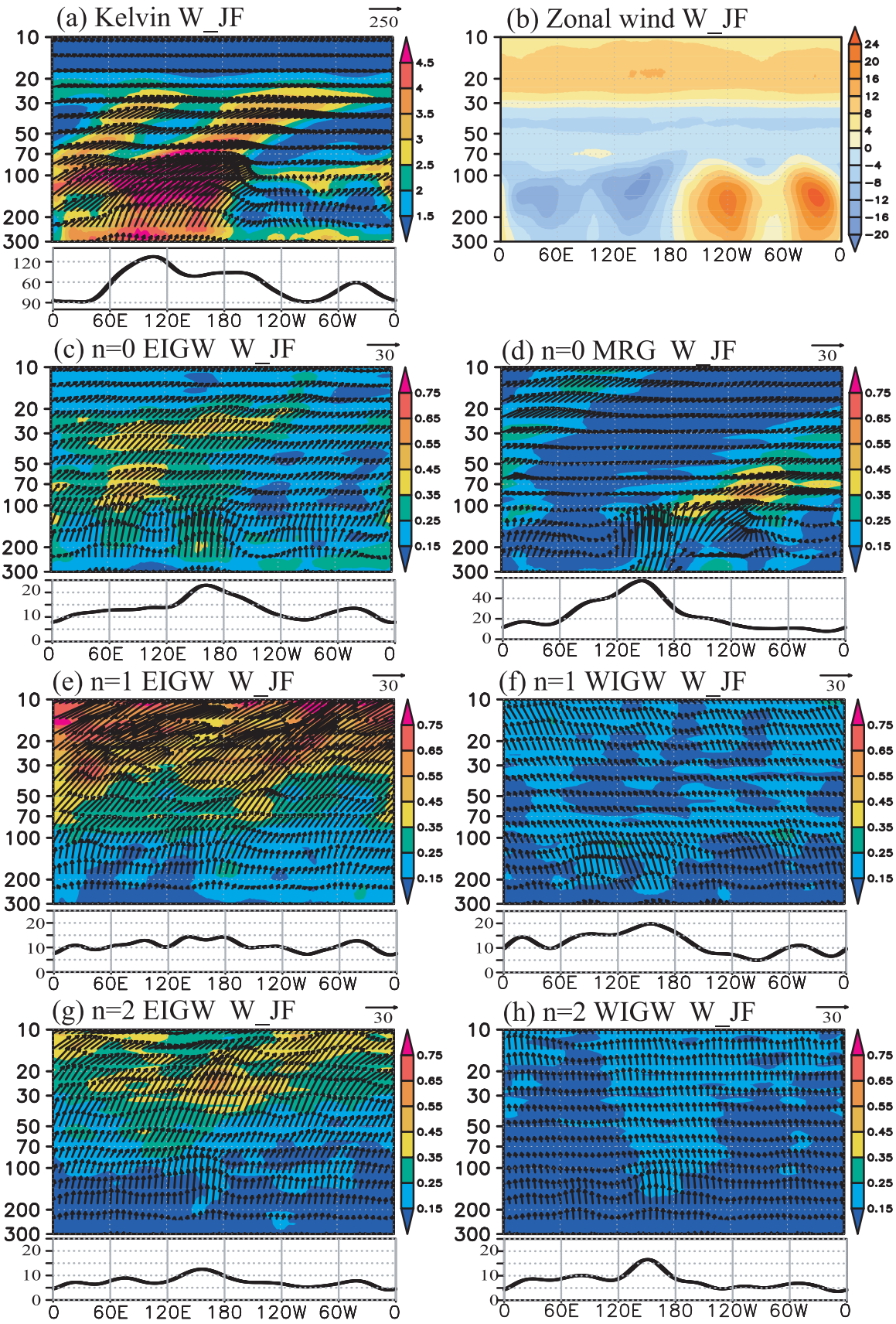
(a) Kelvin W_JF
250
(b) Zonal wind W_JF
(c) n=0 EIGW W_JF
30
(d) n=0 MRG W_JF
30
(e) n=1 EIGW W_JF
30
(f) n=1 WIGW W_JF
30
(g) n=2 EIGW W_JF
30
(h) n=2 WIGW W_JF
30
0 60E 120E 180 120W 60W 0

Figure 10

vertical intrinsic group velocity, respectively. Because the energy fluxes are parallel to the intrinsic group velocity of gravity waves in the context of WKB theory, the sign of energy flux shows the direction of gravity wave propagation relative to the mean wind.

[44] Longitude-height cross-sections of PE and zonal/vertical energy flux ($\overline{\phi' u'}$, $\overline{\phi' w'}$) in Jan–Feb during the westerly and easterly shear phases of the QBO are shown in Figures 10 and 11, respectively (10°S–10°N average). Note that energy fluxes are 2-monthly averaged pictures that should look different at any given time. The line graph indicates the zonal variation in OLR variance due to each wave component averaged from 10°N to 10°S (note the different ranges of the ordinate axes for Kelvin waves, MRG waves, and other EQWs). The top right panel shows the 2-monthly mean and 10°S–10°N average zonal wind.

[45] PE associated with Kelvin waves is most dominant among EQWs (note that the shading intervals in Figures 10 and 11 are different between PE associated with Kelvin waves and those associated with other EQWs). In the troposphere, there are large sources of Kelvin waves in the eastern hemisphere, and most Kelvin waves generated in the eastern hemisphere propagate into the stratosphere (Figures 10a and 11a). Kelvin waves are also excited in the western hemisphere, but energy fluxes suddenly become weak below 100 hPa. These results indicate that the vertical shear of the Walker circulation in the western hemisphere prevents most Kelvin waves from entering the stratosphere by the same mechanism (critical-level filtering) presented in Figure 5. Interestingly, some Kelvin waves generated at approximately 180°E propagate eastward and encounter the westerly in the troposphere at approximately 170–150°W. The value of the energy flux decreases rapidly in the zonal direction. These results indicate that Kelvin waves dissipate not only via vertical propagation, but also via zonal propagation [*Fujiwara and Takahashi*, 2001; *Suzuki and Shiotani*, 2008].

[46] In the westerly shear phase of the QBO, most Kelvin waves in the eastern hemisphere propagate from the troposphere into the middle stratosphere, and their propagation becomes much weaker around 20–30 hPa (Figure 10a), when the QBO is in the westerly phase. On the other hand, in the easterly shear phase, most of the Kelvin waves stop propagating vertically within the range of the westerly phase of the QBO around 50 hPa (Figure 11a). These different propagation characteristics result in the different global distributions of PE around the altitude at which the zonal wind approaches zero (see Figures 6c and 6d).

[47] Even in the westerly shear phase of the QBO (Figure 10a), some Kelvin waves in the eastern hemisphere seem to dissipate around 70 hPa, where zonal wind is nearly 0 m s^{-1} (2-month mean zonal wind averaged from 10°S–10°N is shown in Figure 10b, but there are some areas where zonal wind is positive over the equator; see the vertical profiles of zonal wind with standard deviations shown in Figure 5a). Spectral analysis indicates that very slow Kelvin waves with Cx < ~5 m s^{-1} dissipate around 70–100 hPa (not shown).

[48] From equations (9) and (10), the intrinsic group velocities $\hat{C}gx$ and $\hat{C}gz$ of each EQW can be estimated after calculating both potential energy and kinetic energy due to each EQW. Note that the 2-monthly mean intrinsic group velocity averaged for the spectral domain in zonal wave number-frequency extracted by the equatorial wave filter can be estimated. Here we mention the case of Kelvin waves in the westerly shear phase of the QBO (Figure 10a). The estimated $\hat{C}gx$ and $\hat{C}gz$ in the eastern hemisphere at 70–30 hPa within 10°S–10°N are approximately 25 m s^{-1} and 1.2×10^{-2} m s^{-1}, respectively (not shown). During 5.7 days, the wave packet propagates an estimated ~12,000 km (108°) in the zonal and ~5.9 km (the distance from 70 to 30 hPa) in the vertical direction relative to the mean wind. The direction of energy flux shown in Figure 10a is consistent with this estimation.

[49] In contrast to Kelvin waves, PE due to MRG waves is large in the western hemisphere in the UTLS region. It is interesting that most MRG waves generated from the Indian Ocean to the western Pacific do not enter the stratosphere, despite the large sources (Figures 10d and 11d). The easterly associated with the Walker circulation filters most of the MRG waves in the upper troposphere. MRG waves generated at approximately 150°E–150°W propagate eastward and upward, and contribute to the PE in the stratosphere; note that the intrinsic zonal phase velocity $\hat{C}x$ of MRG waves is negative (i.e., westward), while the intrinsic zonal group velocity $\hat{C}x$ of MRG waves is positive (i.e., eastward). In contrast to Kelvin waves, more MRG waves propagate into the middle stratosphere (up to ~20 hPa) during the easterly shear phase of the QBO (Figure 11d). In this phase, some MRG waves reach approximately 0–30°E in the stratosphere. Careful examination of Figure 6d indicates an off-equatorial PE distribution at approximately 30°W–30°E. MRG waves contribute to the PE around this region.

[50] In the westerly shear phase, most of the $n = 0$ EIGWs propagate until 20–30 hPa (Figure 10c), where the zonal wind is 0–8 m s^{-1}, and generate large PE at this altitude. In the easterly shear phase, some $n = 0$ EIGWs are influenced by the westerly at 70–30 hPa, but more $n = 0$ EIGWs seem to propagate toward the upper stratosphere (Figure 11c), in contrast to Kelvin waves. This is because $n = 0$ EIGWs generally have faster Cx values than Kelvin waves, which can pass through weak westerly zones. These results may be

Figure 10. Longitude-height cross-sections of PE and zonal and vertical energy fluxes ($\overline{\phi' u'}$, $\overline{\phi' w'}$) due to each EQW in the westerly shear phase in Jan–Feb (10°N–10°S average). PE due to (a) Kelvin waves, (c) $n = 0$ EIGWs, (d) MRG waves, (e) $n = 1$ EIGWs, (f) $n = 1$ WIGWs, (g) $n = 2$ EIGWs, and (h) $n = 2$ WIGWs averaged between 10°N and 10°S. (b) Zonal wind averaged from 10°N to 10°N. The line graph indicates zonal variation in OLR variance (W^2 m^{-4}) due to each EWQ component. Note the different ranges of the ordinate axes for Kelvin waves, MRG waves, and other EQWs. The arrow unit is 250 J kg^{-1} m s^{-1} for (a) and 30 J kg^{-1} m s^{-1} for (c–h). The vertical component of energy flux is multiplied by a factor of 1000 to coincide with their direction parallel to the propagation of wave path. The shading interval is 0.5 J kg^{-1} for (a) and 0.1 J kg^{-1} for (c–h). The shading interval is 4 m s^{-1} for zonal wind for (b).

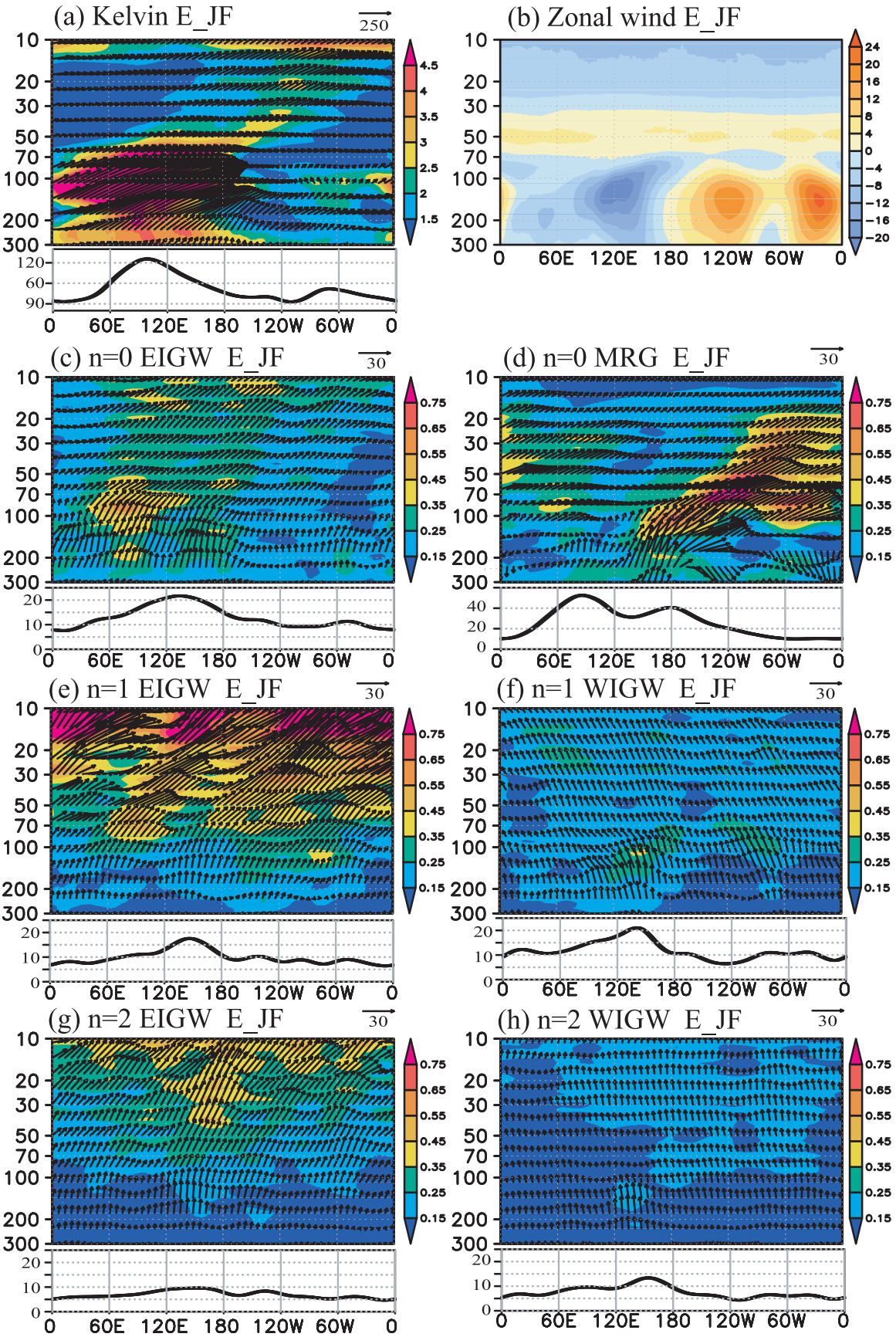

Figure 11. The same as Figure 10, but for the easterly shear phase in Jan–Feb.

dependent on the strength of the background zonal winds, which have seasonal and interannual variation.

[51] Around 70–30 hPa, more $n = 1$ WIGWs propagate into the middle stratosphere in the easterly shear phase (Figure 11f) than in the westerly shear phase of the QBO (Figure 10f), as for MRG waves. However, in general, $n = 1$ and $n = 2$ EIGWs/WIGWs are not influenced much by the background zonal wind (Figures 10e–10h and 11e–11h) to the same extent as Kelvin waves and $n = 0$ EQWs because $n = 1$ and $n = 2$ EIGWs/WIGWs generally have larger Cx with zonal wave numbers ranging from 1 to 9 (see Figure 8; the gradient between the zonal wave number versus the frequency is proportional to Cx). There is also a clear correspondence of wave generation in the troposphere and wave sources for $n = 1$ and $n = 2$ EQWs. For example, the maximum upward propagation of $n = 1$ and $n = 2$ WIGWs in the troposphere occurs at approximately 120–180°E, where the sources of these waves are large.

[52] Waves with larger Cx may interact with the SAO, whereas some $n = 1$ and $n = 2$ waves with relatively small Cx should interact with the QBO. As clearly illustrated in this section, the distributions of stratospheric PE caused by EQWs are greatly affected by the source distribution, the Walker circulation, and the QBO phase. Therefore the stratospheric variation (e.g., interannual and seasonal variation) of PE should be associated with tropospheric variation [*Tsuda et al.*, 2008] in addition to the QBO phase. The simulation results should serve as useful information to gain a better understanding of the observed PE distribution.

4.3. Ratio Between EQWs and 3D-Gravity Waves

[53] The PE associated with EQWs has equatorially trapped structures (Figure 9), and most PE associated with 3D-gravity waves must show no mode to the equator. The PE $\leq$ 7 km shown in Figure 6 is the sum of EQWs $\leq$ 7 km and 3D-gravity waves $\leq$ 7 km. In this section, we discuss investigation of the extent to which EQWs and/or 3D-gravity waves contribute to the PE $\leq$ 7 km. To assess this question in accurate detail, the equatorial-wave filter discussed in section 4.2 was used for temperature data with vertical wavelengths $\leq$ 7 km ($T' \leq$ 7 km). In calculating the temperature associated with EQWs, overlaps between Kelvin waves and $n = 1$ EIGWs and between $n = 0$ EIGWs and $n = 2$ EIGWs were avoided. That is, a Kelvin and $n = 1$ EIGW, $n = 1$ WIGW, and $n = 1$ equatorial Rossby wave filter was applied for the symmetric component of $T' \leq$ 7 km and an MRG wave, $n = 0$ and $n = 2$ EIGW, $n = 2$ WIGW, and $n = 2$ equatorial Rossby wave filter was applied for antisymmetric $T' \leq$ 7 km. The PE $\leq$ 7 km associated with EQWs was then calculated. Here PE values associated with 3D-gravity waves were regarded as the residual of total PE $\leq$ 7 km minus the PE $\leq$ 7 km associated with EQWs.

[54] Figure 12 shows the global distribution of PE $\leq$ 7 km, PE associated with EQWs $\leq$ 7 km, 3D-gravity waves $\leq$ 7 km, and PE associated with EQWs divided by total PE $\leq$ 7 km at 20–30 km (~57–15 hPa) in Jan–Feb during the westerly and easterly shear phases of the QBO. PE $\leq$ 7 km is generally larger in the westerly than in the easterly shear of the QBO (Figures 12a and 12b). The PE with EQWs $\leq$ 7 km is also larger in the westerly shear phase with dominant symmetric structures. On the other hand, in the easterly shear phase, off-equatorial structures of PE with EQWs $\leq$ 7 km were clearly seen around 0–60°E and 0–160°W due to the small activity of Kelvin waves in the easterly shear phase, as discussed in section 4.2. The north-south extent of EQWs is described by the equatorial radius of deformation y_0 as follows:

$$y_0 = \sqrt{N/|m|\beta} = \sqrt{N\lambda_z/2\pi\beta} \tag{11}$$

The amplitude of EQWs becomes $1/\sqrt{e}$ where $y = y_0$ (y is the meridional axis, and y = 0 at the equator; see *Andrews et al.* [1987]). The value of y_0 for EQWs with vertical wavelength of 7 km is approximately 1100 km. Therefore PE (as a function of T'^2) associated with EQWs $\leq$ 7 km should be reduced to less than $1/e \approx 37\%$ within 1100 km. For example, PE with a value of ~3 (J kg^{-1}) in the westerly shear phase over the middle Pacific decreases to a value of approximately ~1.2 (J kg^{-1}) around 10°N (Figure 12c), which is consistent with the estimated meridional range.

[55] PE with 3D-gravity waves $\leq$ 7 km shows a scattered structure with a wide meridional range (Figures 12e and 12f). Large values are observed over areas that include the Congo basin, South America, the Indian Ocean to the mid-Pacific, and northern Australia. GPS RO data also show localized PE, such as over South America [*Tsuda et al.*, 2000, 2008; *Alexander et al.*, 2008b], most likely due to 3D-gravity waves. In Jul–Aug, large PE due to 3D-gravity waves $\leq$ 7 km is distributed around the Indian monsoon region (not shown) in association with large amounts of precipitation (Figure 2d), which is also consistent with GPS RO measurements made by the Challenging Mini-Payload (CHAMP) satellite as described by *Tsuda et al.* [2008].

[56] Of the total PE at 20–30 km, approximately 30% from the Indian Ocean to the eastern Pacific is contributed by EQWs $\leq$ 7 km (Figures 12g and 12h) over the equator, indicating that 3D-gravity waves $\leq$ 7 km contribute ~70% to PE $\leq$ 7 km at this altitude. The contribution of EQWs becomes smaller away from the equator. The contribution of EQWs to PE is smaller over the Atlantic Ocean. In the stratosphere, the ratio in the westerly shear phase is generally larger than in the easterly shear phase of the QBO due to greater propagation of Kelvin waves, which have the largest amplitude of T' among EQWs. The latitude-height cross-section of the ratio averaged between 10°S and 10°N in both Jan–Feb and Jul–Aug reaches up to 40% at the altitude where Kelvin wave activity is large (not shown).

[57] The model covers a much wider spectral range than those in COSMIC GPS RO data as mentioned in section 4.1. This is one possible reason why simulated total PE $\leq$ 7 km was generally larger than that in COSMIC. In fact, the strength of PE $\leq$ 7 km associated with EQWs (Figures 12c and 12d) was comparable to PE with an equatorially trapped structure observed in COSMIC GPS RO data [*Alexander et al.*, 2008b].

[58] The periods of the simulated QBO were shorter than those in the real atmosphere, which implies overestimation of simulated gravity wave activity. *Kawatani et al.* [2005] calculated the simulated net $\overline{u'w'}$ and absolute value of $|\overline{u'w'}|$ (i.e., $|\overline{u'w'}|$ with eastward waves plus $|\overline{u'w'}|$ with westward waves) with periods less than 3 days using the same AGCM as in this study. They compared simulated values with radiosonde observations from Singapore

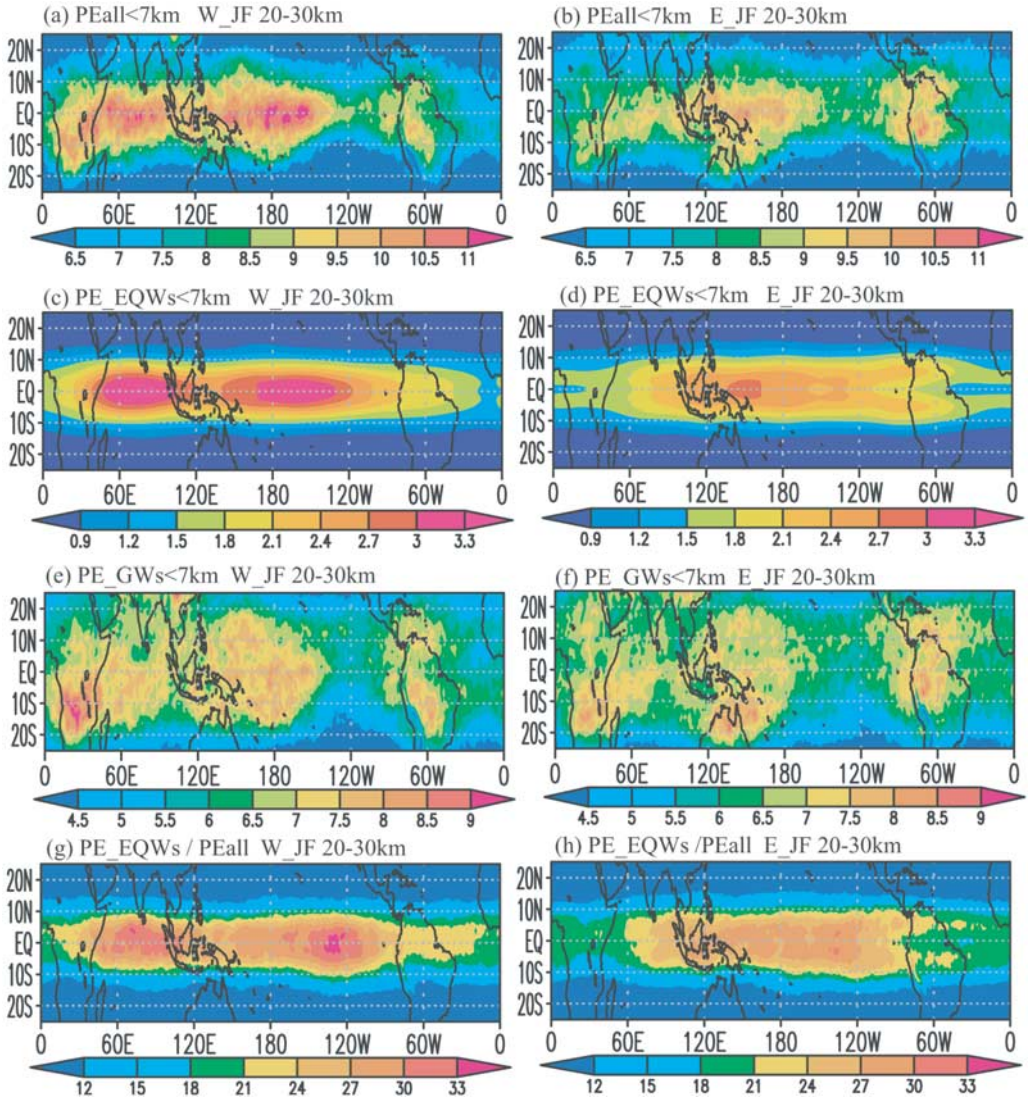

Figure 12. (a, b) Global distribution of total PE with vertical wavelength $\leq$ 7 km at 20–30 km in Jan–Feb. The PE due to (c, d) EQW $\leq$ 7 km components and (e, f) 3D-gravity wave components $\leq$ 7 km. (g, h) The ratio between total PE $\leq$ 7 km and PE due to EQWs $\leq$ 7 km. The left and right panels show the westerly and easterly shear phases of the QBO, respectively. The shading intervals are 0.5 J kg^{-1} for (a, b, e, f), 0.3 J kg^{-1} for (c, d), and 3% for (g, h).

reported by *Sato and Dunkerton* [1997] and confirmed that the simulated $\overline{u'w'}$ and $|\overline{u'w'}|$ were quantitatively in good agreement with the observational results. *Kawatani et al.* [2005] also revealed that simulated $\overline{u'w'}$ has strong longitudinal variation. More observations of gravity waves at different stations are needed to verify the model results.

4.4. Gravity Waves With Periods $\leq$ 24 Hours

[59] As noted in section 1, *Tsuda et al.* [2000] reported large PE over the tropical Atlantic Ocean, and *Kawatani et al.* [2003] concluded that the source of this PE was 3D-gravity waves generated by a diurnal cycle of convection around the Bay of Guinea. Relatively large PE was also simulated over the Amazon and Indonesia. *Kawatani et al.* [2003] presented results obtained in only 1 week of June. In this section, gravity waves with periods $\leq$ 24 h for 2-monthly means in Jan–Feb and Jul–Aug are investigated during the easterly shear phase of the QBO. Note that the 24-h cycle has a repeatable well-defined phase at each point, whereas intraday variance arises from short-lived disturbance at any time of the day. Gravity waves with periods $\leq$ 24 h are generated by both the diurnal cycle of convection and another intraday variability. We extracted wave components by applying a high-pass filter with a cut-off period of 24 h. The terms of the applied cosine-type window and the extracted terms are the same as those explained in section 4.2. The high-pass filter was applied to temperature, geopotential height and wind components to obtain PE $\leq$ 24 h and energy flux $\leq$ 24 h. Note that the vertical wavelength filter was not applied.

[60] Figure 13 shows the 2-monthly mean amplitudes of cumulus precipitation with periods $\leq$ 24 h for Jan–Feb and Jul–Aug during the easterly shear phase of the QBO (different from the previous figures, the starting point of

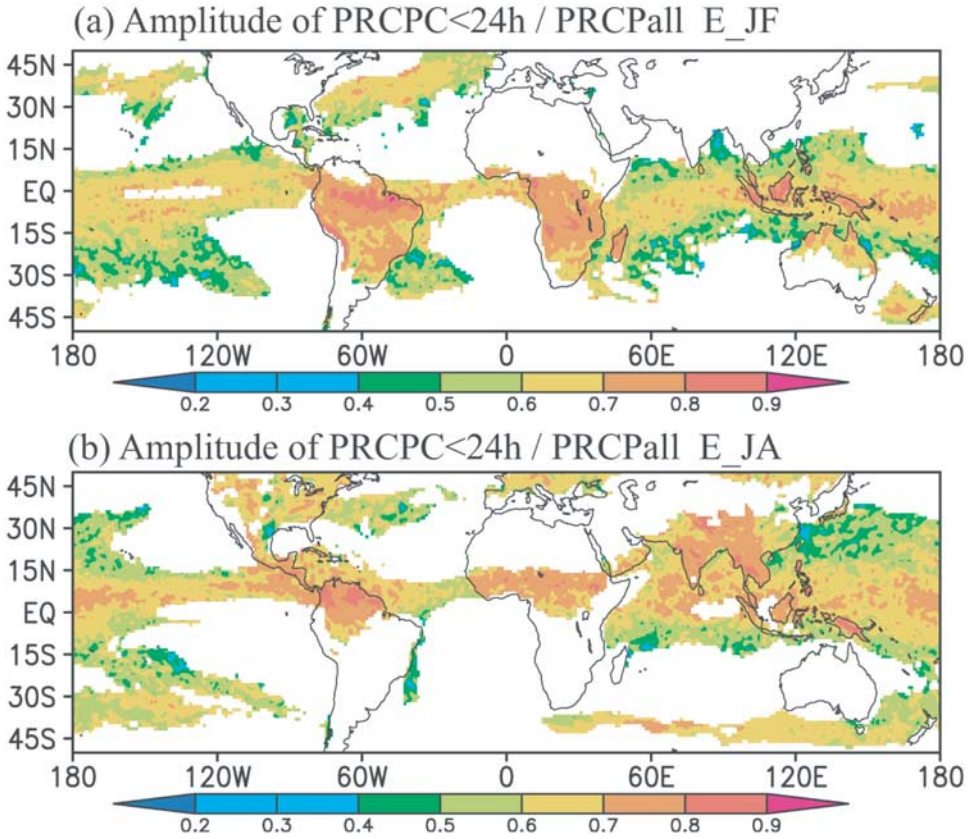

Figure 13. Amplitude of cumulus convection with periods $\leq$ 24 h for (a) Jan–Feb and (b) Jul–Aug during the easterly shear phase of the QBO. Values indicate the ratio between precipitation with periods $\leq$ 24 h and that with periods > 24 h where the 2-monthly mean values of convective precipitation are $\geq$1 mm day^{-1}.

longitude is 180°W). The values indicate the ratio of precipitation amplitude with periods $\leq$ 24 h to that with periods > 24 h. The ratio was calculated when the 2-monthly mean convective precipitation exceeded 1 mm day^{-1}. Cumulus precipitation $\leq$ 24 h includes not only 24 h, but also 6- to 23-h components. Spectral analysis of cumulus convection $\leq$ 24 h over the land indicated a dominant period at 24 h, with a secondary maximum at 12 h. We also calculated the amplitude of cumulus precipitation with periods including only 12-h and 24-h components. In this case, the amplitude became much smaller over the ocean. Regions with strong amplitudes of cumulus convection $\leq$ 24 h are located over South America, the Congo Basin, and around Indonesia in Jan–Feb, and over South America, the Bay of Guinea, and the India, Indochina, and Indonesia region in Jul–Aug. Therefore gravity waves $\leq$ 24 h should be excited over these regions. *Ricciardulli and Sardeshmukh* [2002] used satellite-observed blackbody temperature (TBB) data to show the amplitude of the diurnal cycle of convection relative to the long-term mean. The simulated distributions in the present study were similar to their results.

[61] Figure 14 shows PE $\leq$ 24 h at 100–60 and 35–15 hPa in Jan–Feb and Jul–Aug during the easterly shear phase of the QBO, as well as the three dimensional (3-D) energy fluxes ($\phi'u'$, $\phi'v'$, $\phi'w'$) $\leq$ 24 h at 100–60 and 60–35 hPa. Horizontal energy fluxes were vectored (the points of origin for the energy fluxes show the strength, position, and propagating direction of gravity waves, and the arrowheads do not show the reaching point of a gravity wave) and vertical energy fluxes with values of more than 0.2 (J Kg^{-1} m s^{-1}) are shaded. For example, if an area shows southwestward vectors with shading, gravity waves propagate southwestward and upward on average. Therefore global three-dimensional propagation of gravity waves $\leq$ 24 h can be seen in Figure 14.

[62] In Jan–Feb, there were three localized strong PE areas over South America, the Congo Basin, and around Indonesia at 100–60 hPa, while in Jul–Aug, localized PE was observed over South America. the Bay of Guinea and the Indian monsoon region. These results correspond well to the distribution of the amplitude of cumulus precipitation $\leq$ 24 h (Figure 13). The 3D-gravity waves generated in these areas propagate three-dimensionally and contribute large PE to the stratosphere in areas a short distance from the source region. (Although figures are not shown here we checked the properties of three-dimensional propagation both in zonal-vertical and in meridional-vertical cross-sections of energy fluxes). For example, energy fluxes indicate that large PE at 35–15 hPa around South America is due to 3D-gravity waves generated convectively over the Amazon. Gravity waves with periods of 24 h can propagate until 30°N or 30°S when background zonal winds are zero. The dominant period of the gravity waves generated over land is 24 h, as mentioned above. Therefore most gravity waves

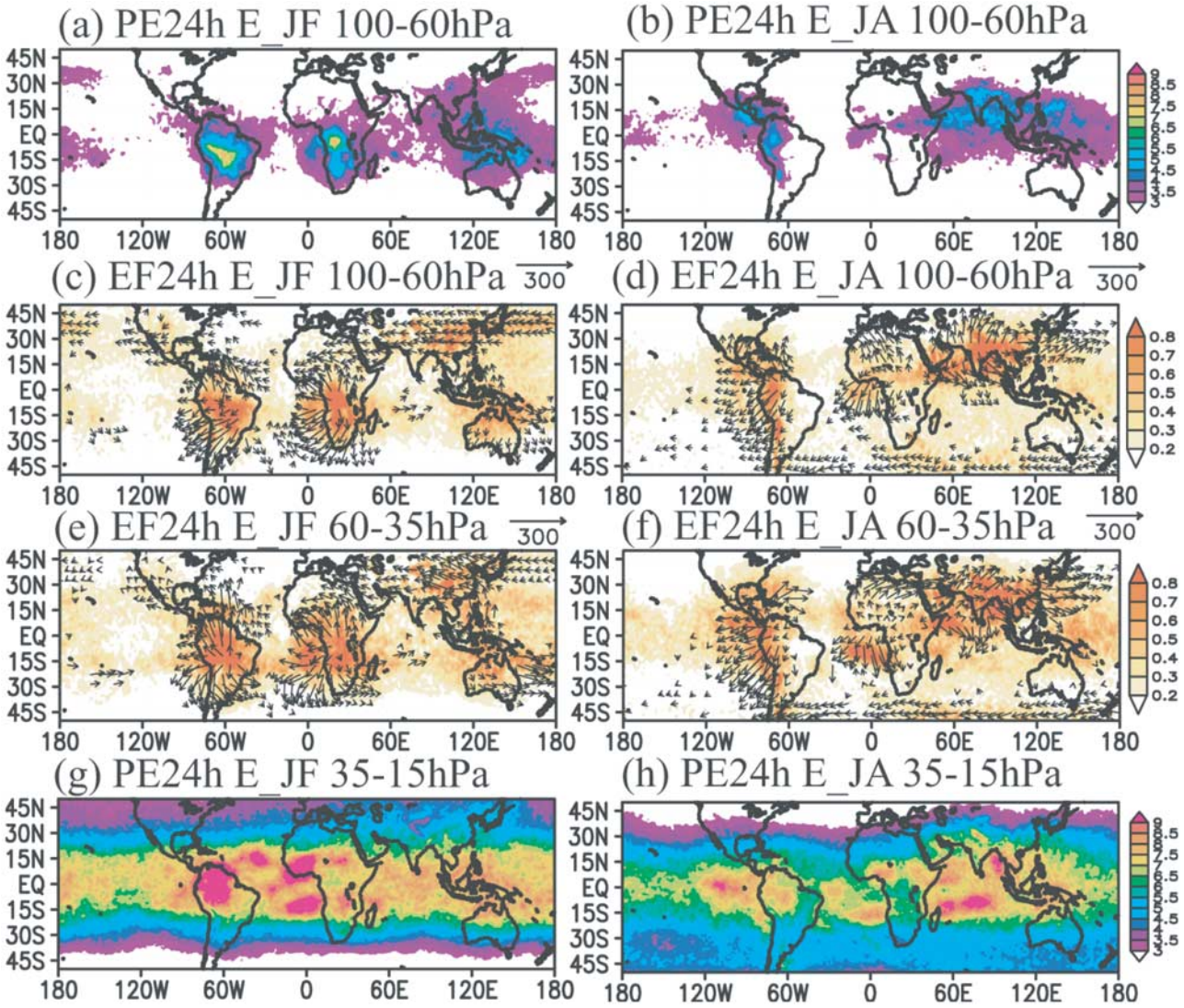

Figure 14. PE with periods $\leq$ 24 h at (a, b) 100–60 hPa and (g, h) 35–15 hPa, and three-dimensional energy fluxes ($\overline{\phi' u'}$, $\overline{\phi' v'}$, $\overline{\phi' w'}$) $\leq$ 24 h at (c, d) 100–60 hPa and (e, f) 60–35 hPa in (left) Jan–Feb and (right) Jul–Aug during the easterly shear phase of the QBO. Horizontal energy fluxes are indicated by vectors, and vertical energy fluxes $\geq$ 0.2 J kg^{-1} m s^{-1} are shaded. The arrow unit is 300 J kg^{-1} m s^{-1}, and horizontal energy fluxes $\geq$ 30 J kg^{-1} m s^{-1} are shown. The shading intervals are 0.5 J kg^{-1} for PE $\leq$ 24 and 0.1 J kg^{-1} m s^{-1} for $\overline{\phi' w'} \leq$ 24 h.

could propagate until 30°N or 30°S and then be reflected to the lower latitudes. Further details were reported previously by *Kawatani et al.* [2003], who described meridional-vertical cross-sections of energy fluxes. We also calculated PE with periods including only 12-h and 24-h components. The PE is relatively large over the lands and areas a short distance from the lands, while the PE becomes much smaller far away from the land such as over the middle Pacific. These results indicated that most PE $\leq$ 24 h over the middle Pacific is due to gravity waves generated by intraday variability, not diurnal cycle of convection.

[63] Interestingly, there were some differences between Jan–Feb and Jul–Aug. In Jul–Aug, as demonstrated by *Kawatani et al.* [2003], convectively generated gravity waves around the Bay of Guinea propagate southwestward across the equator with large upward propagation (Figures 14d and 14f), which results in large PE over the tropical Atlantic Ocean in the stratosphere (Figure 14h). In contrast, in Jan–Feb, a great deal of precipitation occurs over the Congo Basin, rather than the Bay of Guinea (see Figures 2c and 13a). As clearly shown, convectively generated gravity waves around the Congo Basin propagate westward and upward with altitude (Figures 14c and 14e) and then generate large PE over the tropical Atlantic Ocean in the Southern Hemisphere. Therefore the main source of PE over the tropical Atlantic Ocean in Jan–Feb is precipitation over the Congo Basin, which is different in Jul–Aug. Precipitation over the Bay of Guinea makes a secondary contribution to PE over the tropical Atlantic in Jan–Feb.

[64] In Jul–Aug, precipitation $\leq$ 24 h over the Indian monsoon region acts as a strong source of 3D-gravity waves $\leq$ 24 h, and large PE $\leq$ 24 h is distributed in this region

(Figures 14b and 14h). Large PE $\leq$ 7 km is also located over the Indian monsoon region in Jul–Aug (not shown), indicating that Indian monsoon precipitation is a strong source of gravity waves with a wide range of periods. It is also of interest that the propagating directions of gravity waves over the Indian monsoon region are westward in the midlatitudes in Jan–Feb (Figure 14e) and eastward the midlatitudes in Jul–Aug (Figure 14f), which may be responsible for the different background zonal wind directions (i.e., westerly in Jan–Feb and easterly in Jul–Aug).

[65] *Tsuda et al.* [2000] reported localized large PE over the Atlantic, but *Alexander et al.* [2008b] found no distinct large PE in this region, as in our simulated PE $\leq$ 7 km (Figure 12). One possible explanation is that *Tsuda et al.* [2000] selected gravity waves with vertical wavelengths $\leq$ 10 km, whereas *Alexander et al.* [2008b] extracted wave components of $\leq$7 km. *Kawatani et al.* [2003] reported that the vertical wavelengths of gravity waves generated over the Bay of Guinea are 5–10 km, and dominant vertical wavelengths are $\sim$8–10 km. Therefore the different results may reflect the selection of different vertical wavelength ranges. In addition, PE $\leq$ 7 km includes both 3D-gravity waves and EQWs, whereas PE $\leq$ 24 h does not consist of EQWs. This may also explain why isolated PE $\leq$ 24 h is clearly observed over the tropical Atlantic Ocean.

[66] Using an aqua planet AGCM, *Sato et al.* [1999] showed that zonally averaged gravity waves $\leq$ 24 h generated over the equatorial region propagated poleward. The AGCM used here, which included a realistic boundary condition, also showed that gravity waves $\leq$ 24 h generated in the low latitudes generally propagate to higher latitude with height. Global distribution of sources and three-dimensional propagation of gravity waves $\leq$ 24 h obtained in the present study provide additional information regarding where gravity waves are generated and the 3-D direction in which gravity waves propagate (Figures 13 and 14).

5. Summary and Concluding Remarks

[67] We investigated the global distribution, sources, and propagation of EQWs and 3D-gravity waves using the CCSR/NIES/FRCGC AGCM with T106L60 resolution. The QBO-like oscillations with periods of approximately 1.5–2 years were simulated well without gravity-wave drag parameterization. The zonal wave number versus the frequency spectra of simulated precipitation represents realistic signals of convectively coupled EQWs such as Kelvin waves, MRG waves, n = 0 EIGWs, n = 1 equatorial Rossby waves and n = 1 WIGWs. The temperature spectra also revealed the signals of EQWs in the stratosphere.

[68] It appears to have been difficult to detect coherence between the troposphere and stratosphere with equatorial wave observations because the troposphere and stratosphere are very different with regard to statistic stability, presence or absence of latent heating, and mean flow speed. In the present study, each EQW component was extracted using an equatorial wave filter, with fixed spectral ranges in the zonal wave number-frequency domain. Because the ground-based frequency ω and zonal wave number k of a wave do not change unless a wave is dissipated, we were able to investigate the wave propagation properties from the troposphere through the stratosphere.

[69] Each EQW generation generally corresponded well with the source of each convectively coupled EQW activity in the troposphere. The difference in the vertical shear of the Walker circulation between the eastern and western hemispheres plays an important role in wave filtering, which results in different PE distributions between the eastern hemisphere and western hemisphere in the UTLS region. The propagation of Kelvin waves, MRG waves, and n = 0 EIGWs is strongly influenced by the Walker circulation and the phase of the QBO. The distributions of stratospheric PE associated with EQWs are greatly affected by (1) the source distribution, (2) Walker circulation, and (3) QBO phase.

[70] EQWs with vertical wavelength $\leq$ 7 km contribute up to $\sim$30% of total PE $\leq$ 7 km in the stratosphere. Thus 3D-gravity waves $\leq$ 7 km, which do not have a mode to the equator, account for $\sim$70% of the PE $\leq$ 7 km. The minimum simulated horizontal wavelength, vertical wavelength, and period of the simulated 3D-gravity waves are $\sim$380 km, 1.1 km, and 6 h, respectively. The AGCM covers a wide spectrum range of atmospheric waves, which results in larger PE in the AGCM than that observed in COSMIC GPS RO data.

[71] Areas with large amplitudes of cumulus precipitation $\leq$24 h are located over South America, the Congo Basin, and Indonesia in Jan–Feb and over South America, the Bay of Guinea, and the India, Indonesia, and Indochina region in Jul–Aug, which is in good agreement with observations. The 3D-gravity waves generated over these areas contribute to localized PE $\leq$ 24 h at short distances from the source region. There are some differences in the sources, three-dimensional propagation, and global distribution of PE $\leq$ 24 h between Jan–Feb and Jul–Aug.

[72] The model results were essentially consistent with recent results obtained from GPS RO data [*Alexander et al.*, 2008b; *Tsuda et al.*, 2008]. The COSMIC GPS RO data and the AGCM results shared the following characteristics. (1) Much larger PE elongates from east to west over the eastern hemisphere than over the western hemisphere in the UTLS region. (2) Around the altitude where the phase of the QBO changes, zonally nonuniform PE distributions are more apparent in the easterly shear phase than in the westerly shear phase of the QBO. (3) Temperature disturbances associated with Kelvin waves in the stratosphere are generally larger in the eastern hemisphere than in the western hemisphere. (4) MRG waves are more dominant in the westerly shear phase than in the easterly shear phase of the QBO. (5) Large PE $\leq$ 7 km is observed over South America, which should be due to 3D-gravity waves. The mechanisms of these shared characteristics were well explained in the present analysis.

[73] The global distribution of PE depends on the height, background wind (the QBO and the Walker circulation), and wave sources, as was clearly demonstrated in this study. The present study has discussed only four cases in Jan–Feb and Jul–Aug with easterly and westerly shear phases of the QBO (see Figure 1), using an AGCM with a climatological boundary condition. In the real atmosphere, PE in the stratosphere should show distinct interannual and seasonal variation, associated with tropospheric variability, such as El Niño Southern Oscillation (ENSO) events [cf. *Tsuda et*

al., 2008]. *Alexander et al.* [2008b] noted that MRG waves are sometimes active in the eastern hemisphere, as in the western hemisphere, while larger model-simulated MRG waves are distributed mainly in the western hemisphere during analyzed terms. To investigate interannual and seasonal variation of EQWs in the model, analysis over longer periods is required. The modeled zonal wind associated with the Walker circulation is stronger and the simulated QBO has smaller amplitude compared with those in the real atmosphere. A more accurate simulation of the zonal wind in the equatorial region is necessary for a more quantitative evaluation of gravity wave activity.

[74] In this study, we focused on investigating what kinds of waves contribute to the global PE distribution, which can be captured by recent satellite observations. Another interesting question is which EQWs and/or 3D-gravity waves drive the QBO. In addition, many waves also dissipate to the upper part of the Walker circulation (Figures 5, 10, and 11), which implies the interaction between gravity waves and the mean flow. *Kawatani et al.* [2005] showed zonal asymmetry of gravity wave forcing $\leq$ 3 days associated with the vertical derivation of net vertical flux of zonal momentum ($\partial(\overline{u'w'})/\partial z$) in UTLS regions. They indicated that large eastward forcing occurs in the eastern hemisphere, while westward forcing is dominant in the western hemisphere in these regions. Recently, *Watanabe et al.* [2008] conducted a 3-year integration using a much higher resolution CCSR/NIES/FRCGC AGCM (T213L256; from the surface to ~85 km). They reported that the amplitude of the QBO-like oscillation was improved despite showing a shorter period. Further studies using the AGCM in conjunction with observations are required to understand global wave activities.

[75] **Acknowledgments.** We thank T.J. Dunkerton for helpful comments and variable advice on this study. We express our gratitude to J. Austin for editing the manuscript and two anonymous reviewers for constructive comments on the original manuscripts. This study is supported by a grant-in-aid for Young Scientists (B) (20740280) from the Japan Society for the Promotion of Science. The GFD-DENNOU library was used for spectral calculations and drawing figures. GrADS was also used for drawing figures.

References

Alexander, S. P., T. Tsuda, and Y. Kawatani (2008a), COSMIC GPS observations of Northern Hemisphere winter stratospheric gravity waves and comparisons with an atmospheric general circulation model, *Geophys. Res. Lett.*, *35*, L10808, doi:10.1029/2008GL033174.

Alexander, S. P., T. Tsuda, Y. Kawatani, and M. Takahashi (2008b), Global distribution of atmospheric waves in the equatorial upper troposphere and lower stratosphere region: 1. COSMIC observations of wave mean flow interactions, *J. Geophys. Res.*, doi:10.1029/2008JD010039, in press.

Allen, S. J., and R. A. Vincent (1995), Gravity wave activity in the lower atmosphere: Seasonal and latitudinal variations, *J. Geophys. Res.*, *100*, 1327–1350.

Andrews, D. G., J. R. Holton, and C. B. Leovy (1987), *Middle Atmosphere Dynamics*, 489 pp., Academic Press, New York.

Arakawa, A., and W. H. Schubert (1974), Interactions of cumulus cloud ensemble with the large-scale environment. part I, *J. Atmos. Sci.*, *46*, 661–685.

Baldwin, M. P., et al. (2001), The quasi-biennial oscillation, *Rev. Geophys.*, *39*, 179–229.

Bergman, J. W., and M. L. Salby (1994), Equatorial wave activity derived from fluctuations in observed convection, *J. Atmos. Sci.*, *51*, 3791–3806.

Dhaka, S. K., M. Takahashi, Y. Kawatani, S. Malik, Y. Shibagaki, and S. Fukao (2003), On the convective updrafts in generation of the gravity waves during tropical convection events, *J. Meteorol. Soc. Jpn.*, *81*, 1185–1199.

Dunkerton, T. J. (1983), The evolution of latitudinal shear in Rossby gravity wave, mean flow interaction, *J. Geophys. Res.*, *88*, 3836–3842.

Eckermann, S. D., I. Hirota, and W. K. Hocking (1995), Gravity wave and equatorial wave morphology of the stratosphere derived from long-term rocket soundings, *Q. J. R. Meteorol. Soc.*, *121*, 149–186.

Emori, S., T. Nozawa, A. Numaguti, and I. Uno (2001), Importance of cumulus parameterization for precipitation simulation over East Asia in June, *J. Meteorol. Soc. Jpn.*, *79*, 939–947.

Ern, M., P. Preusse, M. Krebsbach, M. G. Mlynczak, and J. M. Russell III (2008), Equatorial wave analysis from SABER and ECMWF temperatures, *Atmos. Chem. Phys.*, *8*, 845–869.

Fritts, D. C., and M. J. Alexander (2003), Gravity wave dynamics and effects in the middle atmosphere, *Rev. Geophys.*, *41*(1), 1003, doi:10.1029/2001RG000106.

Fritts, D. C., and G. D. Nastrom (1992), Sources of mesoscale variability of gravity waves: part I. Frontal, convective, and jet stream excitation, *J. Atmos. Sci*, *49*, 111–127.

Fujiwara, M., and M. Takahashi (2001), Role of the equatorial Kelvin wave in stratosphere-troposphere exchange in a general circulation model, *J. Geophys. Res.*, *106*, 22,763–22,780.

Gill, A. E. (1982), Atmospheric-Ocean dynamics, Academic Press, New York.

Giorgetta, M. A., E. Manzini, and E. Roechner (2002), Forcing of the quasi-biennial oscillation from a broad spectrum of atmospheric waves, *Geophys. Res. Lett.*, *29*(8), 1245, doi:10.1029/2002GL014756.

Hamilton, K. (1991), Climatological statistics of stratospheric inertia-gravity waves deduced from historical rocketsonde wind and temperature data, *J. Geophys. Res.*, *96*, 20,831–20,839.

Hamilton, K., R. J. Wilson, and R. Hemler (1999), Atmosphere simulated with high vertical and horizontal resolution versions of a GCM: Improvement in the cold pole bias and generation of a QBO-like oscillation in the tropics, *J. Atmos. Sci.*, *56*, 3829–3846.

Hamilton, K., R. J. Wilson, and R. Hemler (2001), Spontaneous stratospheric QBO-like oscillations simulated by the GFDLSKYHI general circulation model, *J. Atmos. Sci.*, *58*, 3271–3292.

Hayashi, Y., D. G. Golder, and P. W. Jones (1997), Tropical gravity waves and superclusters simulated by high-horizontal-resolution SKYHI general circulation models, *J. Meteorol. Soc. Jpn.*, *75*, 1125–1139.

Hei, H., T. Tsuda, and T. Hirooka (2008), Characteristics of atmospheric gravity wave activity in the polar regions revealed by GPS radio occultation data with CHAMP, *J. Geophys. Res.*, *113*, D04107, doi:10.1029/2007JD008938.

Hirota, I. (1978), Equatorial waves in the upper stratosphere and mesosphere in relation to the semiannual oscillation of the zonal wind, *J. Atmos. Sci.*, *35*, 714–722.

Hirota, I. (1984), Climatology of gravity waves in the middle atmosphere, *J. Atmos. Terr. Phys.*, *46*, 767–773.

Hitchman, M. H., and C. B. Leovy (1988), Estimation of the Kelvin wave contribution to the semiannual oscillation, *J. Atmos. Sci*, *45*, 1462–1475.

Horinouchi, T., and S. Yoden (1998), Wave-mean flow interaction associated with a QBO-like oscillation simulated in a simplified GCM, *J. Atmos. Sci.*, *55*, 502–526.

Horinouchi, T., T. Nakamura, and J. Kosaka (2002), Convectively generated mesoscale gravity waves simulated throughout the middle atmosphere, *Geophys. Res. Lett.*, *29*(21), 2007, doi:10.1029/2002GL016069.

Horinouchi, T., et al. (2003), Tropical cumulus convection and upward-propagating waves in middle-atmospheric GCMs, *J. Atmos. Sci.*, *60*, 2765–2782.

K-1 Model Developers (2004), K-1 Coupled GCM (MIROC) Description, *K-1 Tech. Rep.*, *1*, pp. 1–34, University of Tokyo, Tokyo, Japan.

Kawatani, Y., S. K. Dhaka, M. Takahashi, and T. Tsuda (2003), Large potential energy of gravity waves over a smooth surface with little convection: Simulation and observation, *Geophys. Res. Lett.*, *30*(8), 1438, doi:10.1029/2003GL016960.

Kawatani, Y., M. Takahashi, and T. Tokioka (2004), Gravity waves around the subtropical jet of the southern winter in an atmospheric general circulation model, *Geophys. Res. Lett.*, *31*, L22109, doi:10.1029/2004GL020794.

Kawatani, Y., K. Tsuji, and M. Takahashi (2005), Zonally non-uniform distribution of equatorial gravity waves in an atmospheric general circulation model, *Geophys. Res. Lett.*, *32*, L23815, doi:10.1029/2005GL024068.

Le Treut, H., and Z.-X. Li (1991), Sensitivity of an atmospheric general circulation model to prescribed SST changes: Feedback effects associated with the simulation of cloud optical properties, *Clim. Dyn.*, *5*, 175–187.

Lin, J.-L., et al. (2006), Tropical intraseasonal variability in 14 IPCC AR4 climate models: part I. Convective signals, *J. Clim.*, *19*, 2665–2690, doi:10.1175/JCLI3735.1.

Madden, R. A., and P. R. Julian (1971), Detection of a 40–50 day oscillation in the zonal wind in the tropical Pacific, *J. Atmos. Sci.*, *28*, 702–708.

Magaña, V., and M. Yanai (1995), Mixed Rossby-gravity waves triggered by lateral forcing, *J. Atmos. Sci.*, *52*, 1473–1486.

Matsuno, T. (1966), Quasi-geostrophic motions in the equatorial area, *J. Meteorol. Soc. Jpn.*, *44*, 25–43.
Mellor, G. L., and T. Yamada (1982), Development of a turbulence closure model for geostrophic fluid problems, *Rev. Geophys.*, *20*, 851–875.
Nakazawa, T. (1988), Tropical super clusters within intraseasonal variations over the western Pacific, *J. Meteorol. Soc. Jpn.*, *66*, 823–839.
Naujokat, B. (1986), An update of the observed quasi-biennial oscillation of the stratospheric wind over the tropics, *J. Atmos. Sci.*, *43*, 1873–1877.
O'Sullivan, D., and T. J. Dunkerton (1995), Generation of inertia-gravity waves in a simulated life cycle of baroclinic instability, *J. Atmos. Sci.*, *52*, 3695–3716.
Preusse, P., A. Dornbrack, S. D. Eckermann, M. Riese, B. Schaeler, J. T. Bacmeister, D. Broutman, and K. U. Grossmann (2002), Space-based measurements of stratospheric mountain waves by CRISTA: 1. Sensitivity, analysis method, and a case study, *J. Geophys. Res.*, *107*(D23), 8178, doi:10.1029/2001JD000699.
Randel, W. J., and F. Wu (2005), Kelvin wave variability near the equatorial tropopause observed in GPS radio occultation measurements, *J. Geophys. Res.*, *110*, D03102, doi:10.1029/2004JD005006.
Ratnam, M. V., G. Tetzlaff, and C. Jacobi (2004), Global and seasonal variations of stratospheric gravity wave deduced from the CHAMP/GPS satellite, *J. Atmos. Sci.*, *61*, 1610–1620.
Ricciardulli, L., and P. D. Sardeshmukh (2002), Local time- and space scales of organized tropical deep convection, *J. Clim.*, *15*, 2775–2790.
Salby, M. L., D. L. Hartmann, P. L. Bailey, and J. C. Gille (1984), Evidence for equatorial Kelvin modes in Nimbus-7 LIMS, *J. Atmos. Sci.*, *41*, 220–235.
Sato, K. (1994), A statistical study of the structure, saturation and sources of inertia-gravity waves in the lower stratosphere observed with the MU radar, *J. Atmos. Terr. Phys.*, *56*, 755–774.
Sato, K., and T. J. Dunkerton (1997), Estimates of momentum flux associated with equatorial Kelvin and gravity waves, *J. Geophys. Res.*, *102*, 26,247–26,261.
Sato, K., and M. Yoshiki (2008), Gravity wave generation around the polar vortex in the stratosphere revealed by 3-hourly radiosonde observations at Syowa Station, *J. Atmos. Sci.*, *65*, 3719–3735, doi:10.1175/2008JAS2539.1.
Sato, K., T. Kumakura, and M. Takahashi (1999), Gravity waves appearing in a high resolution GCM simulation, *J. Atmos. Sci.*, *56*, 1005–1018.
Suzuki, J., and M. Shiotani (2008), Space-time variability of equatorial Kelvin waves and intraseasonal oscillations around the tropical tropopause, *J. Geophys. Res.*, *113*, D16110, doi:10.1029/2007JD009456.
Takahashi, M. (1996), Simulation of the stratospheric quasi-biennial oscillation using a general circulation model, *Geophys. Res. Lett.*, *23*, 661–664.
Takahashi, M. (1999), Simulation of the quasi-biennial oscillation in a general circulation model, *Geophys. Res. Lett.*, *26*, 1307–1310.
Tsuda, T., Y. Murayama, M. Yamamoto, S. Kato, and S. Fukao (1990), Seasonal variation of momentum flux in the mesosphere observed with the MU radar, *Geophys. Res. Lett.*, *17*, 725–728.
Tsuda, T., M. Nishida, C. Rocken, and R. H. Ware (2000), A global morphology of gravity wave activity in the stratosphere revealed by the GPS occultation data (GPS/MET), *J. Geophys. Res.*, *105*, 7257–7273.
Tsuda, T., M. V. Ratnam, S. P. Alexander, T. Kozu, and Y. Takayabu (2008), Temporal and spatial distributions of atmospheric wave energy in the equatorial stratosphere revealed by GPS radio occultation temperature data obtained with the CHAMP Satellite during 2001–2006, *Earth Planets Space*, in press.
Wada, K., T. Nitta, and K. Sato (1999), Equatorial inertia-gravity waves in the lower stratosphere revealed by TOGA-COARE IOP data, *J. Meteorol. Soc. Jpn.*, *77*, 721–736.
Wallace, J. M., and V. E. Kousky (1968), Observation evidence of Kelvin waves in the tropical stratosphere, *J. Atmos. Sci.*, *25*, 900–907.
Watanabe, S., K. Sato, and M. Takahashi (2006), A general circulation model study of orographic gravity waves over Antarctica excited by katabatic winds, *J. Geophys. Res.*, *111*, D18104, doi:10.1029/2005JD006851.
Watanabe, S., Y. Kawatani, Y. Tomikawa, K. Miyazaki, M. Takahashi, and K. Sato (2008), General aspects of a T213L256 middle atmosphere general circulation model, *J. Geophys. Res.*, *113*, D12110, doi:10.1029/2008JD010026.
Wheeler, M., and G. N. Kiladis (1999), Convectively coupled equatorial waves: Analysis of clouds and temperature in the wave number-frequency domain, *J. Atmos. Sci.*, *56*, 374–399.
Wheeler, M., G. N. Kiladis, and P. J. Webster (2000), Large-scale dynamical fields associated with convectively coupled equatorial waves, *J. Atmos. Sci.*, *57*, 613–640.
Wu, D. L., and J. W. Waters (1996), Satellite observations of atmospheric variances: A possible indication of gravity waves, *Geophys. Res. Lett.*, *23*, 3631–3634.
Xie, P., and P. A. Arkin (1996), Analyses of global monthly precipitation using gauge observations, satellite summaries, and numerical model predictions, *J. Clim.*, *9*, 840–858.
Yanai, M., and T. Maruyama (1966), Stratospheric wave disturbances propagating over the equatorial Pacific, *J. Meteorol. Soc. Jpn.*, *44*, 291–294.
Yoshiki, M., and K. Sato (2000), A statistical study of gravity waves in the polar regions based on operational radiosonde data, *J. Geophys. Res.*, *105*, 17,995–18,011.

S. P. Alexander and T. Tsuda, Research Institute for Sustainable Humanosphere, Kyoto University, Gokasho, Uji, Kyoto 611-0011, Japan.
Y. Kawatani and M. Takahashi, Frontier Research Center for Global Change, Japan Agency for Marine-Earth Science and Technology, 3173-25 Showamachi, Kanazawa-ku, Yokohama City, Kanagawa 236-0001, Japan. (yoskawatani@jamstec.go.jp)
K. Sato, Department of Earth and Planetary Science, Graduate School of Science, University of Tokyo, 7-3-1, Hongo, Bunkyo-ku, Tokyo 113-0033, Japan.